International Journal of Plasticity 159 (2022) 103462

Contents lists available at ScienceDirect

International Journal of Plasticity

journal homepage: www.elsevier.com/locate/ijplas

# A peridynamic approach to solving general discrete dislocation dynamics problems in plasticity and fracture: Part II. Applications

Wenbo Dong [a], Hengjie Liu [a], Juan Du [b], Xu Zhang [c], Minsheng Huang [a,d,*], Zhenhuan Li [a,d], Ziguang Chen [a,d,*], Florin Bobaru [e]

[a] Department of Engineering Mechanics, School of Aerospace Engineering, Huazhong University of Science and Technology, Wuhan 430074, China
[b] Science and Technology on Reactor System Design Technology Laboratory, Nuclear Power Institute of China, Chengdu 610213, China
[c] School of Mechanics and Aerospace Engineering, Southwest Jiaotong University, Chengdu 610031, China
[d] Hubei Key Laboratory of Engineering Structural Analysis and Safety Assessment, 1037 Luoyu Road, Wuhan 430074, China
[e] Department of Mechanical and Materials Engineering, University of Nebraska-Lincoln, Lincoln, NE 68588-0526, USA

ARTICLE INFO

*Keywords:*
Discrete dislocation dynamics
Peridynamics
Plasticity
Indentation
Fracture
Hall-Petch effect

ABSTRACT

In Part II of this work we extend the method introduced in Part I to consider dislocation dynamic evolution through dislocations nucleation, glide, pile-up, and annihilation. The SP DDD-PD scheme is employed to investigate uniaxial tension in a single crystal and a polycrystal and verify its accuracy. The model is then used to simulate elastoplastic fracture by considering interactions between dislocations and crack growth. For Mode I elastoplastic fracture in a single crystal, we observe that the crack path is "attracted" towards regions of high density of gliding dislocations, leading to an undulating crack paths, as observed in experiments but never replicated by continuum-level computational models before. Tests on different sample sizes show how the proximity of constraints to the crack tip can lead to plastic hardening. Ductile-to-brittle transition happens naturally in this model when the crack, under Mode I displacement-controlled loading, approaches a free edge. A new way to calibrate the critical bond strain based on the material toughness or fracture energy is proposed. The present SP DDD-PD scheme can be used to investigate complicated elastoplastic fracture problems in which the interaction between dislocation motion and damage is critical.

## 1. Introduction

As a physics-based theory and a computational tool, Discrete Dislocation Dynamics (DDD) has been applied to simulate the dynamic evolution of discrete dislocations during mechanical deformation and phase transformation in crystalline materials. DDD is usually coupled with other methods, such as the finite element method (FEM) (Cleveringa et al., 1999; Cui et al., 2022; Guo et al., 2021; Longsworth and Fivel, 2021; Lu et al., 2022; Wang et al., 2022), extended finite element method (XFEM) (Belytschko and Gracie, 2007; Liang et al., 2021; Oswald et al., 2011), boundary element method (BEM) (El-Awady et al., 2008; Takahashi and Ghoniem, 2008), etc., to solve elastoplastic Boundary Value Problems (BVPs). Among these methods, the one using the FEM method has a relatively strong dependence on the computational mesh (Campilho et al., 2011; Cornejo et al., 2020; Song et al., 2022; Wang

* Corresponding authors at: Department of Engineering Mechanics, School of Aerospace Engineering, Huazhong University of Science and Technology, Wuhan 430074, China.
*E-mail addresses:* mshuang@hust.edu.cn (M. Huang), zchen@hust.edu.cn (Z. Chen).

https://doi.org/10.1016/j.ijplas.2022.103462
Received 20 July 2022; Received in revised form 27 September 2022;
Available online 18 October 2022

et al., 2019b). When coupled with the XFEM, the extended form function must be used, making the model considerably more cumbersome. Special techniques are needed for using the BEM-based model to solve problems with inhomogeneous microstructures that involve larger-scale samples (El-Awady et al., 2008). Moreover, since the methods mentioned above (FEM, XFEM, and BEM) are all based on the continuity assumption, requiring extra algorithmic conditions on how damage/cracks form from dislocations and special rules/techniques for redefining the body, remeshing, etc. altogether leading to drastic limitations for analyzing the microscopic fracture behavior of materials. This, perhaps, is the main reason for which no attempts have been made so far to simulate the dislocation to crack transition problem. To date, in dislocation-based studies of elastoplastic fracture, fracture paths generally are preset, e.g., as straight segments (Liang et al., 2019). However, experimental evidence shows tortuous fracture surfaces in single crystals (Creuziger et al., 2008; Kalácska et al., 2020; Sumigawa et al., 2018). To tackle this problem and study the interaction between dislocations and propagating cracks, new DDD models that allow cracks to grow autonomously need to be introduced. This is the topic of the present paper.

As a reformulation of classical mechanics, peridynamics (PD) is based on replacing spatial derivatives from the classical models with integral operators (Silling, 2000). In this way, cracks are allowed to naturally initiate and propagate autonomously, leading to results that match experimental observations in a variety of fracture and damage problems in a variety of materials (Xu et al., 2018; Zhang et al., 2018). Due to its great advantages in dealing with displacement discontinuities, PD has been widely used in a variety of material degradation and damage cases, such as quasi-static and dynamic brittle and ductile fracture, thermally-driven fracture, corrosion and stress corrosion cracking (Chen and Bobaru, 2015; Chen et al., 2021; Cheng et al., 2022; Mousavi et al., 2021; Wu et al., 2021, 2020; Xu et al., 2018), etc.

In Part I of this work (Dong et al., 2022), a superposition (SP) scheme of peridynamic and discrete dislocation dynamics (DDD) (i.e., SP DDD-PD scheme) was developed to study boundary value problems (BVPs) with dislocations and various types of damage (pores, cracks) embedded. By replacing the classical surface traction in the complementary problem, and the complementary problem itself, with a nonlocal/peridynamic one, the SP DDD-PD scheme can simulate arbitrary domains, including those with pre-damage, cracks, and voids of arbitrary shapes, without explicitly tracking boundaries, interfaces, cracks, etc. This scheme has been employed to simulate the interaction between multiple dislocations, solve the stress field around a dislocation emitted from a crack tip, and model the interaction between dislocation and voids. All dislocations considered in Part I (Dong et al., 2022) were stationary. In this second part of the work, the SP DDD-PD scheme is employed to simulate dislocation-based elastoplastic response in both single and polycrystals. The simulation results are compared with those from DDD-FEM and DDD-XFEM, to further verify the feasibility and accuracy of the proposed SP DDD-PD method for the evolution of dislocations in elasto-plastic problems. We then use the new method to calculate the dislocation/stress evolution during elastoplastic indentation and mode-I fracture in single-crystal metals.

## 2. The SP DDD-PD scheme for elastoplastic and fracture problems

In Part I of this work (Dong et al., 2022), the DDD was reviewed briefly, and the superposed (SP) scheme of DDD and PD was introduced. The solution of the SP DDD-PD scheme includes the deformation fields ($\sim$) for dislocations embedded in an isotropic infinite body and the complementary correction fields ($\hat{}$) used to satisfy the given boundary conditions. The overall responses for the BVPs can be written as

$$\boldsymbol{u} = \widetilde{\boldsymbol{u}} + \widehat{\boldsymbol{u}}, \boldsymbol{\varepsilon} = \widetilde{\boldsymbol{\varepsilon}} + \widehat{\boldsymbol{\varepsilon}}, \boldsymbol{\sigma} = \widetilde{\boldsymbol{\sigma}} + \widehat{\boldsymbol{\sigma}} \tag{1}$$

where $\boldsymbol{u}$, $\boldsymbol{\varepsilon}$, and $\boldsymbol{\sigma}$ are the total displacement, strain and stress fields, respectively.

Different from Part I (Dong et al., 2022), where stationary dislocations embedded in single crystals and polycrystals with voids/cracks were considered, here, in Part II, we focus on BVPs with quasi-static displacement boundary conditions, but in which we follow the dislocation dynamic evolution, such as dislocations' glide, nucleation, motion, pile-up and annihilation. The elastoplastic response obtained will be a direct result of dislocation glide, and long-range and short-range interactions between dislocations. The long-range dislocation interaction is governed by the Peach-Koehler (P-K) force, and the short-range interactions are modelled by a series of constitutive laws, which are briefly reviewed as follows.

The Peach-Koehler (P-K) force (Peach and Koehler, 1950) controls the motion of dislocations. In DDD, it can be represented as (Van der Giessen and Needleman, 1995):

$$f^i = n^i \cdot \left( \widehat{\sigma} + \sum_{j \neq i} \widetilde{\sigma}^j \right) \cdot b^i \tag{2}$$

where $\boldsymbol{n}^i$ is the unit normal of the slip plane, $\widehat{\sigma}$ is the stress of the supplementary problem, $\widetilde{\sigma}^j$ represents the stress induced by all other dislocations on the considering dislocation $i$, and $\boldsymbol{b}^i$ the Burgers vector. The glide velocity $\boldsymbol{v}^i$ of the $i$th dislocation can be calculated by the P-K force as:

$$\boldsymbol{v}^i = \frac{\boldsymbol{f}^i}{B} \tag{3}$$

where $B$ is the Drag coefficient set as $B = 10^5$ Pa·ns (Kubin et al., 1992), which is a representative value for typical FCC crystals, including aluminum, the material considered in this work.

In this paper, the dislocation nucleation is simulated based on the Frank-Read source (Frank and Read Jr, 1950). No dislocation is

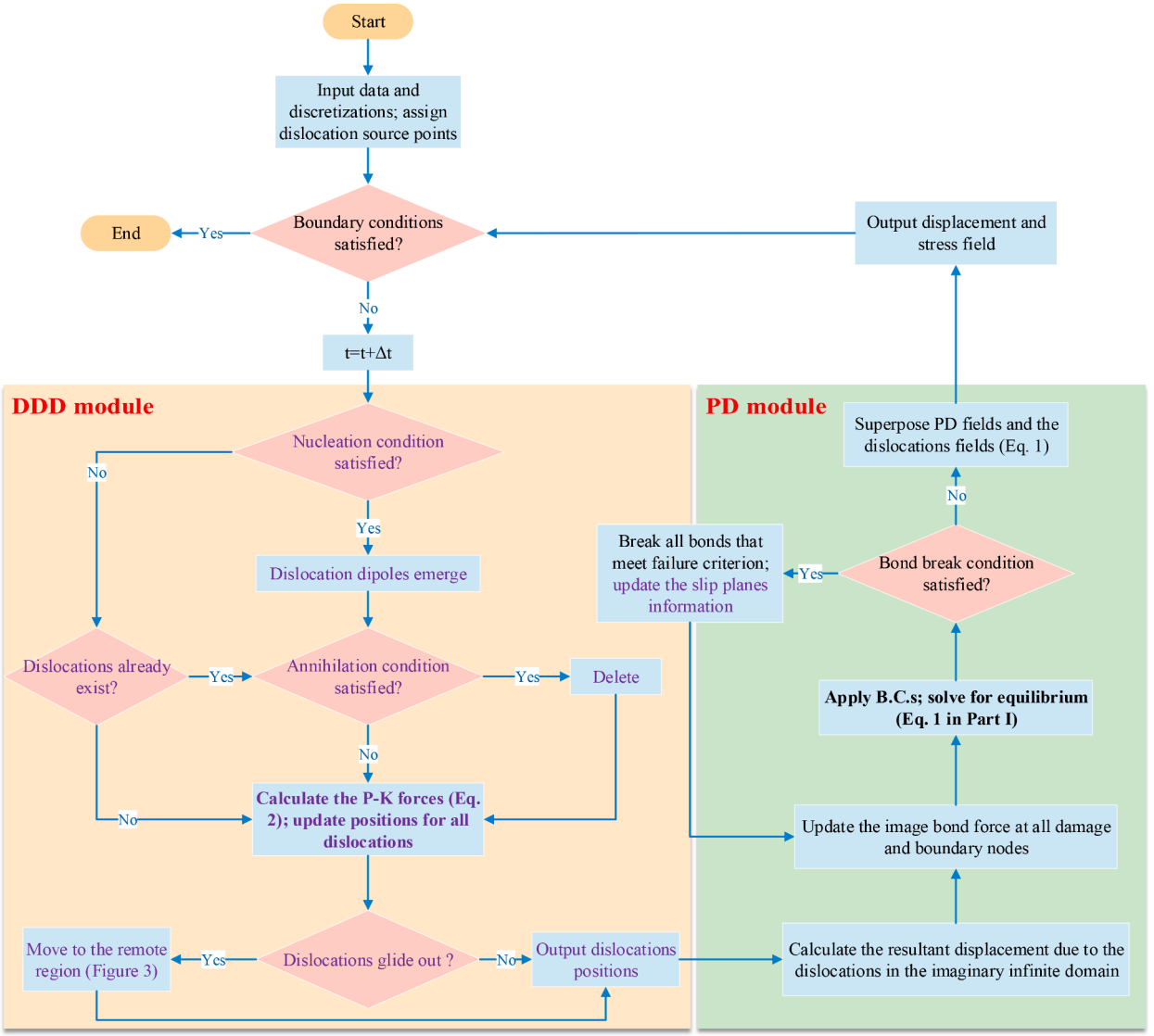


**Fig. 1.** Flow-process diagram of SP DDD-PD method for dislocation-based elastoplastic deformation and fracture.

introduced initially. Initial dislocation source points are distributed randomly on the slip planes. The single crystal selected in this work is face-centered cubic (FCC) aluminum. For the 2D plane-strain case considered, three slip systems are included. For each slip system, a series of slip planes are distributed with a uniform spacing of 100$b$, with $b$ being the magnitude of the Burgers vector.

When the effective shear stress at the considering source point exceeds the critical nucleation stress within a time period$t_{nuc}$ (Van der Giessen and Needleman, 1995), a pair of dislocation dipoles with opposite Burgers vectors form near the dislocation source. When the distance between two opposite dislocations on the same slip plane is less than the critical distance 6$b$, they annihilate each other.

The computational flow of the SP DDD-PD scheme for BVPs with dislocation evolutions is shown in Fig. 1. The major components are the DDD module and the PD module. The DDD module controls the dislocation nucleation, motion, pile-up, escaping from surfaces and annihilation. The PD module is employed to solve for equilibrium with the given boundary conditions. After each time step, the dislocations information is updated in the DDD module and then transferred to the PD module, when conditions require. By using the PD model and the superposition scheme, the stress, displacement fields, and damage evolution can be computed (for more details, please refer to Part I (Dong et al., 2022)). The updated stress and damage information is then transferred back to the DDD module for the simulation of the next time step.

Note the PD module in the DDD-PD model is for small deformation calculations. However, the DDD-PD model is composed of two modules: the DDD module and the PD module. The plastic strain is calculated in the DDD module, and it accumulates during the calculation steps. During each step, the accumulated strain is small, but over many steps, plastic strains can accumulate to large values.

Suddenly applied constant-rate displacement-controlled boundary conditions are considered in this work. The effect of strain rate

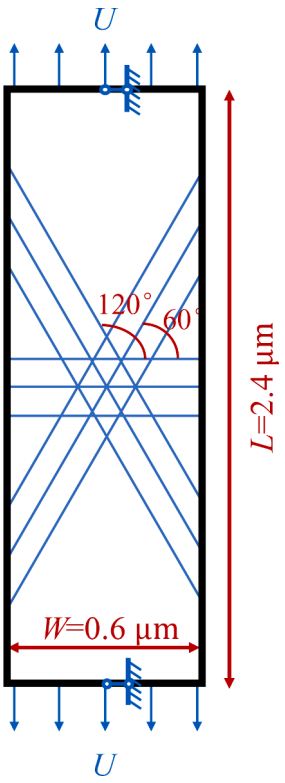


**Fig. 2.** Loading conditions and slip planes distribution in the uniaxial tension test of single-crystal aluminum sample (rigid-body rotation is removed by constraining the horizontal displacement for the middle points on the top and bottom sides).

on both the mechanical behavior and dislocation evolution is investigated. In computations, the strain rate$\dot{\varepsilon}$ is adjusted by varying the elongation increment ($\Delta l$) along the loading direction (with original length$L_o$):

$$\dot{\varepsilon} = \frac{\Delta l}{L_o}\frac{1}{\Delta t} \tag{4}$$

where$\Delta t$ is the time step set as$\Delta t = 0.5$ ns (Balint et al., 2008; Deshpande et al., 2003). The strain rates considered in this work are in the range of 200∼1000 $s^{-1}$. Although this strain rate is much higher than values achieved under quasi-static experimental conditions at the macro-scale, the static PD solver is still suitable since the sample size is only about 1∼10 μm, inducing loading rates 5∼6 orders of magnitude lower than the dislocation speed and the elastic wave speed. Therefore, in this work, the DDD module is dynamic, but the PD solver is quasi-static.

In the following sections, the developed SP DDD-PD scheme is employed to simulate the elastoplastic uniaxial tension (under plane strain conditions) of a single crystal (Section 3) and polycrystal (Section 4), indentation of a rigid rectangular beam on a single crystal structure (Section 5), and crack growth in a single crystal under Mode I fracture (Section 6).

## 3. Uniaxial tension of single crystal

As shown in Fig. 2, a rectangular model with a geometry of0.6 $\mu$m × 2.4 $\mu$m, under plane-strain condition, is considered. For the peridynamic computations, the horizon size (the distance limit within which a material point directly interacts with other points in the peridynamic model, see Part I (Dong et al., 2022) for details) is chosen as$\delta = 0.0402$ μm, and the horizon factor $m$ (the ratio between the horizon size and grid spacing, see Dong et al. 2022 for details) is set as 4.02, leading to about 16,864 nodes in the uniform grid. The material is single-crystal aluminum, with Young's modulus $E = 70$ GPa and Poisson's ratio$\nu = 0.25$, corresponding to plane-strain conditions in bond-based PD. The magnitude of Burgers vector is taken to be $b = 0.25$ nm, and the friction for the dislocation glide is set to zero. Three slip systems in directions 0°, 60°, 120° (with respect to the x-axis positive direction, see Fig. 2) are distributed in the model (Deshpande et al., 2003; Huang et al., 2007). The distance for the neighboring slip planes is set to $100b = 25$ nm for each slip system.

At the initial stage, the deformation is linearly elastic and no dislocation nucleates, meaning that at this stage, the computational solution is solely completed by the PD algorithm. Although no dislocations exist in the material initially, dislocation sources are randomly distributed. The density of the dislocation sources is chosen as$\rho = 50/\mu m^2$ similar to those used by (Balint et al., 2008; Van der Giessen and Needleman, 1995). Once the density of dislocation sources becomes large enough, the dislocation nucleation rate is

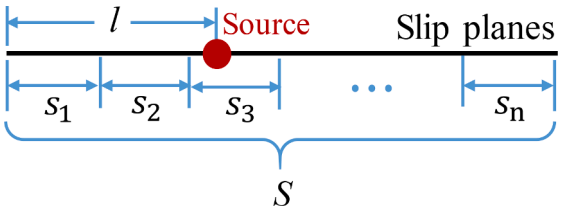


**Fig. 3.** Defining the location of a dislocation source point.

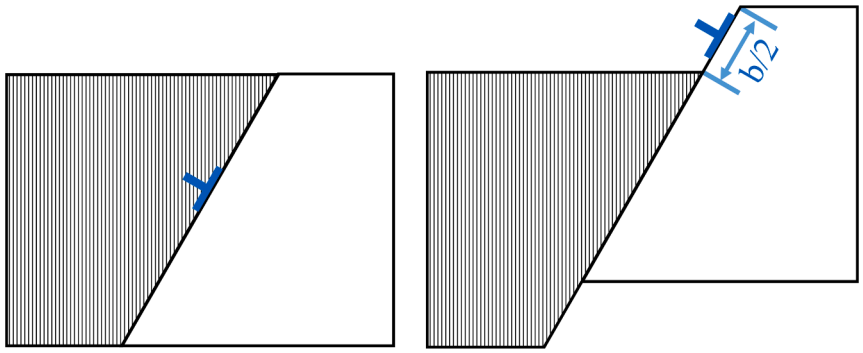


**Fig. 4.** Displacement produced by a dislocation gliding out of an undamaged model.

roughly determined by the dislocation-source strength and independent of the source density. In addition, the hardening behavior and yield strain of the material is slightly affected by the source density, but the yield and flow strength are not affected.

To distribute dislocation sources randomly in the model with the desired density, we use the following algorithm:

(1) Setup slip planes for dislocation motion. Generate starting point coordinates ($\boldsymbol{x}_{0i}$) of each slip plane, the length of each slip plane$s_i$ (the $i$th slip plane), and compute the total length $S$ of slip planes (see Fig. 3. $S=\sum_{i=1}^{n} s_i$, where $n$ is the total number of slip planes);
(2) Calculate the total number of the source points ($N$), which is$0.6\ \mu\text{m} \times 2.4\ \mu\text{m} \times 50\ /\mu\text{m}^2 = 72$ in the problem considered in Fig. 2;
(3) Generate a random number ($R$) in the interval from 0 to 1;
(4) Multiply the random number ($R$) by the total slip planes' length $S$ (the summation of all the slip planes' lengths) to obtain a length value$l = S \times R$. Then, a specific slip plane (the $j$-th slip plane) is determined to satisfy:$\sum_{i=1}^{j-1} s_i \le l < \sum_{i=1}^{j} s_i$. The coordinates of a source point are:$\boldsymbol{x}_{s1} = \boldsymbol{x}_{0i} + (l - \sum_{i=1}^{j-1} s_i)\frac{\boldsymbol{b}^j}{b^j}$ (as shown in Fig. 3);
(5) Repeat steps (3) and (4) $N$-1 times.

Note that source points' locations are set to be not too close to the free boundary to avoid dislocations induced by the meshing-related stress concentration. For this, if a source point obtained according to the above algorithm has a distance from the boundary less than a horizon size, the source point will be eliminated, and a new source point will be generated at another place.

The strength of a dislocation source$\tau_{\text{nuc}}$ follows a Gaussian distribution, with a mean value$\overline{\tau}_{\text{nuc}} = 50$ MPa and a standard deviation $0.2\overline{\tau}_{\text{nuc}} = 10$ MPa. When the magnitude of the P-K force at the dislocation source exceeds$\tau_{\text{nuc}} b$ during a time step of 10 ns, a pair of dislocation dipoles nucleate near the source.

Once a dislocation reaches the surface (boundary of the sample), the dislocation can glide out from the model. Although this dislocation disappears and no longer produces stress field in the material, it induces a permanent deformation field in the material. As a result, a surface step equal to the magnitude of Burgers vector $\boldsymbol{b}$ is introduced, as shown in Fig. 4. The deformed model can be regarded as two rigid regions divided by the dislocation slip plane.

When no damage (such as cracks) is present (see examples in Sections 3–5), dislocations only glide out from the sample's surfaces. However, when damage initiates and evolves in the material, a dislocation can glide out from the newly formed crack's surfaces, for example. More detail about how to deal with dislocation escaping at a newly created surface is given in Section 6.

A uniaxial tension test is carried out using the new SP DDD-PD scheme with different loading rates of$\dot{\varepsilon} = 200$/s, 500/s, and 1000/s. Imposed displacements are applied on both upper and lower boundaries of the simulation model, and the "mirror-type" method (Mei et al., 2021) of imposing Dirichlet boundary conditions in a PD model is adopted. The left and right sides of the sample are traction free (see Fig. 2). In addition, the $x$ coordinates of upper and lower center points are fixed to prevent rigid body rotations. For each simulation case, the model is loaded until the strain reaches 2%. To verify the present SP DDD-PD scheme, we compare results with those from the SP DDD-FEM scheme (with implementation following (Huang et al., 2007)), with node spacing and the DDD parameters

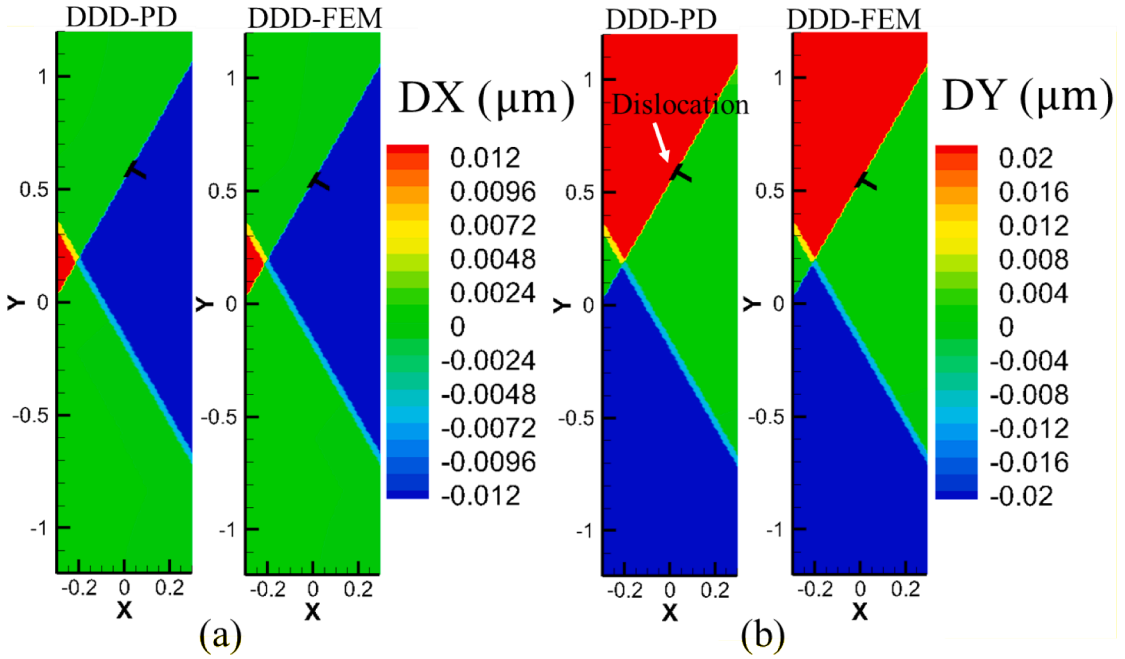


**Fig. 5.** (a) Horizontal and (b) vertical displacements at strain $\varepsilon = 2\%$, obtained from the DDD-PD and DDD-FEM models. Strain rate $\dot{\varepsilon} = 200/s$. The units for both the coordinates and displacements shown are μm.

set similarly to those used in the SP DDD-PD scheme.

The numerical displacement and stress fields at the applied strain$\varepsilon = 2\%$ obtained with the SP DDD-PD and the SP DDD-FEM schemes are plotted in Fig. 5 and Fig. 6, respectively. These figures show that although the dislocation source points are randomly distributed throughout the modeling region, most dislocations nucleate from two slip planes. The reason is that once a dislocation nucleates, it shields the activation of other sources and guides subsequent dislocations to nucleate on the same slip planes. The first nucleated dislocations and the corresponding glide planes create specific spots of stress concentration to guide the nucleation of the follow-up dislocations. The results by the present SP DDD-PD scheme match well with those by the SP DDD-FEM scheme. The only noticeable differences are in the stress fields (the calculation method of stress fields in PD is shown in Appendix C in Part I of this work (Dong et al., 2022)) near the bottom-right corner of the sample (see Fig. 6). These are caused by the PD surface effect (Le and Bobaru, 2018).

The stress contours at$\varepsilon = 2\%$ and the achieved stress-strain curves are given in Fig. 7 and Fig. 8, respectively, for different loading rates. When the strain rate$\dot{\varepsilon}$ equals to 200/s (see Fig. 6) or 500/s (see Fig. 7a), the dislocations have enough time to glide out of the crystal; only one dislocation can be observed for the considered strain. In contrast, for a strain rate of 1000/s, more dislocations co-exist simultaneously in the crystal (see Fig. 7b).

The stress-strain curves calculated with the SP DDD-PD and DDD-FEM schemes and shown in Fig. 8, exhibit an elastic perfectly-plastic behavior (linear elasticity/constant stress plasticity). The stresses from the DDD-PD model are obtained by multiplying the sum of bond force density in Y-direction$f_y$ of the $m$-layer nodes above the upper boundary (within the thickness of$\delta$) by the square of node spacing and then dividing by the width of the model (Lehoucq and Silling, 2008; Wu et al., 2020). The stresses from the DDD-PD model are obtained by dividing the sum of the stress values$\sigma_{yy}$ of the nodes in the upper boundary layer by the number of nodes.

The yield stress$\sigma_Y$ shown in Fig. 8 follows the Schmid law:$\sigma_Y = \frac{1}{u}\tau_{nuc}$, where the Schmid factor $u$ for the 2D case is$\frac{1}{2}\sin 2\theta$ ($\theta$ is the angle between the loading and slip directions), and the mean value of the dislocation source strength$\tau_{nuc}$ is 50 MPa. With$\theta = 30^\circ$, we obtain the yield stress of about 115.5 MPa. This value is close to the stresses at the peaks (corresponding to the nucleation of dislocations) of the curves in Fig. 8. Peak stresses for different strain rates are almost the same, but the low-points of the fluctuations decrease with increasing strain rate. This is because more dislocations nucleate simultaneously at the higher strain rates, leading to larger drops and wider stress fluctuations.

The slightly higher flow stress values calculated by PD-DDD compared to those calculated by the FEM-DDD are due to the combination of nonlocality and numerical discretization methods used. For example, the meshfree method used in the PD model discretization is equivalent to a piecewise constant discontinuous Galerkin FEM, which has lower accuracy than bilinear finite elements used in the FEM solution. New ways to calculate highly accurate (closer to the classical solution) stresses from PD models and formulate new models for dislocation evolution based on deformations or displacements only, may be possible, and this will be studied in the future.

In the single crystal tension case, the dislocation density is related to the sample size, strain rate, setting of obstacles, etc. (Deshpande et al., 2005) shows that the dislocation density depends strongly on the sample size, and the dislocation density decreases

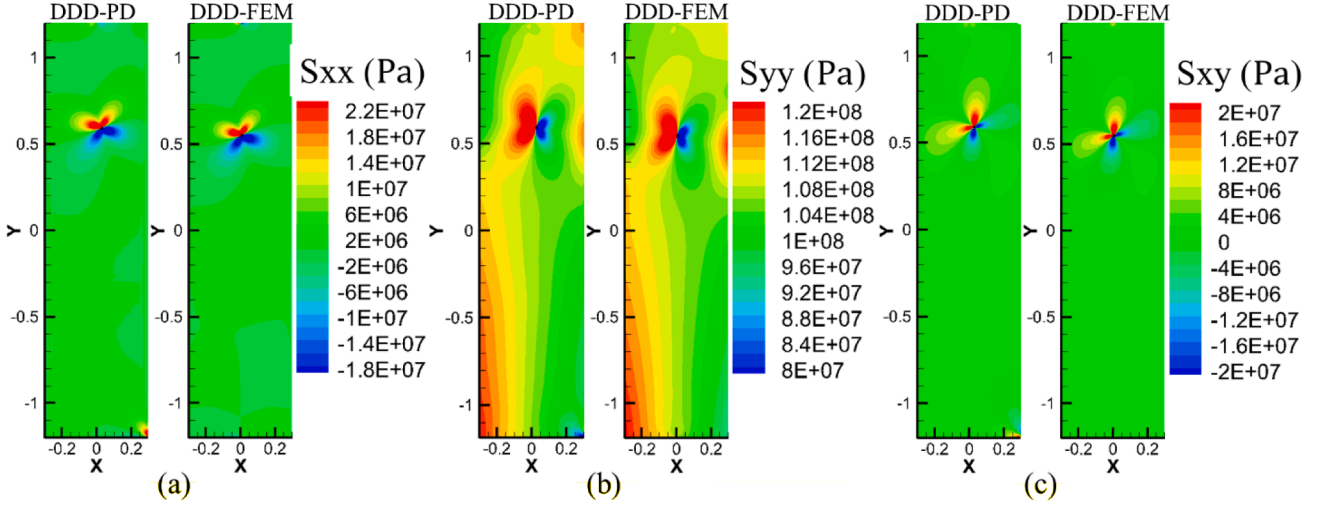


**Fig. 6.** The stress fields (a) $\sigma_{xx}$, (b) $\sigma_{yy}$, and (c) $\sigma_{xy}$ calculated with DDD-PD and DDD-FEM. Strain rate $\dot{\varepsilon} = 200/s$. The unit of the color bars is Pa for stresses.

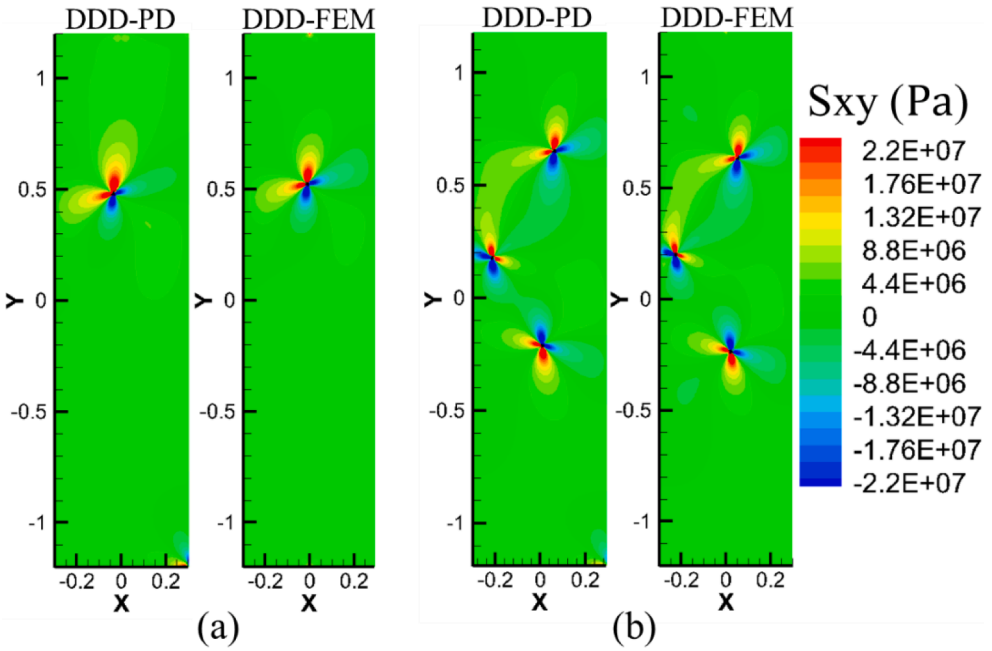


**Fig. 7.** The $\sigma_{xy}$ stress fields for tensile tests with strain rates: $\dot{\varepsilon} = 500/s$ (a), and $\dot{\varepsilon} = 1000/s$ (b), calculated with the DDD-PD and DDD-FEM.

with decreasing size. The smaller the strain rate, the smaller the number of dislocations nucleates in each time step. One way to look at more "complex" cases is to add obstacles that prevent dislocation motion. In Appendix A and Section 4, we show how rigid boundaries affect the dislocation evolution during uniaxial tension.

## 4. Uniaxial tension of polycrystal with rigid grain boundaries

Dislocations could be hindered by other material defects (including other dislocations). Grain boundaries (GBs) are defects that can block dislocations effectively. In this section, we apply the SP DDD-PD scheme to simulate uniaxial tension of polycrystalline aluminum, similar to the cases studied in Huang et al. (2020) using the DDD-XFEM model, to further validate its applicability on dislocation problems.

Due to the presence of GBs, mechanical properties of polycrystals are usually different from those of a single crystal (Hirth, 1972; Thompson et al., 1973). The dependence of mechanical properties on the grain size usually follows the Hall-Petch law, i.e., the yield strength increases with decreasing grain size (Hall, 1951a, b; Sylwestrowicz and Hall, 1951).

For this simulation, we set the GBs as rigid boundaries, that is, dislocation can neither penetrate the GBs nor be reflected or absorbed by the boundaries. This case is the same as the one in (Huang et al., 2020). The cases with penetrable GBs can also be simulated by the present SP DDD-PD, but this is not pursued in this paper.

Fig. 9 shows the polycrystalline aluminum sample composed of$4 \times 12$ grains, also considered, in Huang et al. (2020), where the DDD-XFEM scheme was used. The grains are all squares with a side length $d$. The elastic modulus, Poisson's ratio, and magnitude of Burgers vector are the same as those for the single crystals used in the last section. The source density is$\rho = 80/\mu m^2$, similar to Huang et al. (2020). As shown in Fig. 9, slip systems 2 and 3 have an intersection angle of 54.736°, counterclockwise and clockwise, respectively, from the slip system 1 (Huang et al., 2020). The grain orientation depends on the direction of slip system 1, which is distributed randomly in each grain. Therefore, the entire polycrystalline sample considered in Fig. 9 can be treated, statistically, as isotropic and homogeneous.

A constant strain rate$\dot{\varepsilon} = 500/s$ along Y direction is applied suddenly to both the upper and lower boundary. The left and right boundaries are traction free. As a result, dislocations can freely glide out from the left and right boundaries. Note that no dislocation sources are placed in the bottom and top layers of grains to simulate the gripper effect. This setting is consistent with that used in (Huang et al., 2020). The dislocation gliding away from free surfaces is similar to the cases discussed above, that is, a dislocation is deleted from the model and a permanent displacement is set along the slip plane (Segurado et al., 2007).

For the single crystal case, we have demonstrated in Part I (Dong et al., 2022) that the present DDD-PD model has good-$\delta$-convergence (Bobaru et al., 2009) properties. Here we test its convergence behavior for the polycrystalline case, and obtain stress~strain curves for$\delta = 0.2$, 0.1, 0.08, and 0.05 μm shown in Fig. 10, for the fixed grain size $d = 0.25$ μm. A bilinear elastoplastic behavior can be observed for all four$\delta$ considered, and for both the elastic and plastic regimes, results are consistent with each other. Fig. 10 indicates that a horizon size in the range between 0.05 and 0.2 μm does not appear to influence the results.

Note that for the single crystal case, the stress-strain relationship obtained by the model was also bilinear but with a perfectly-

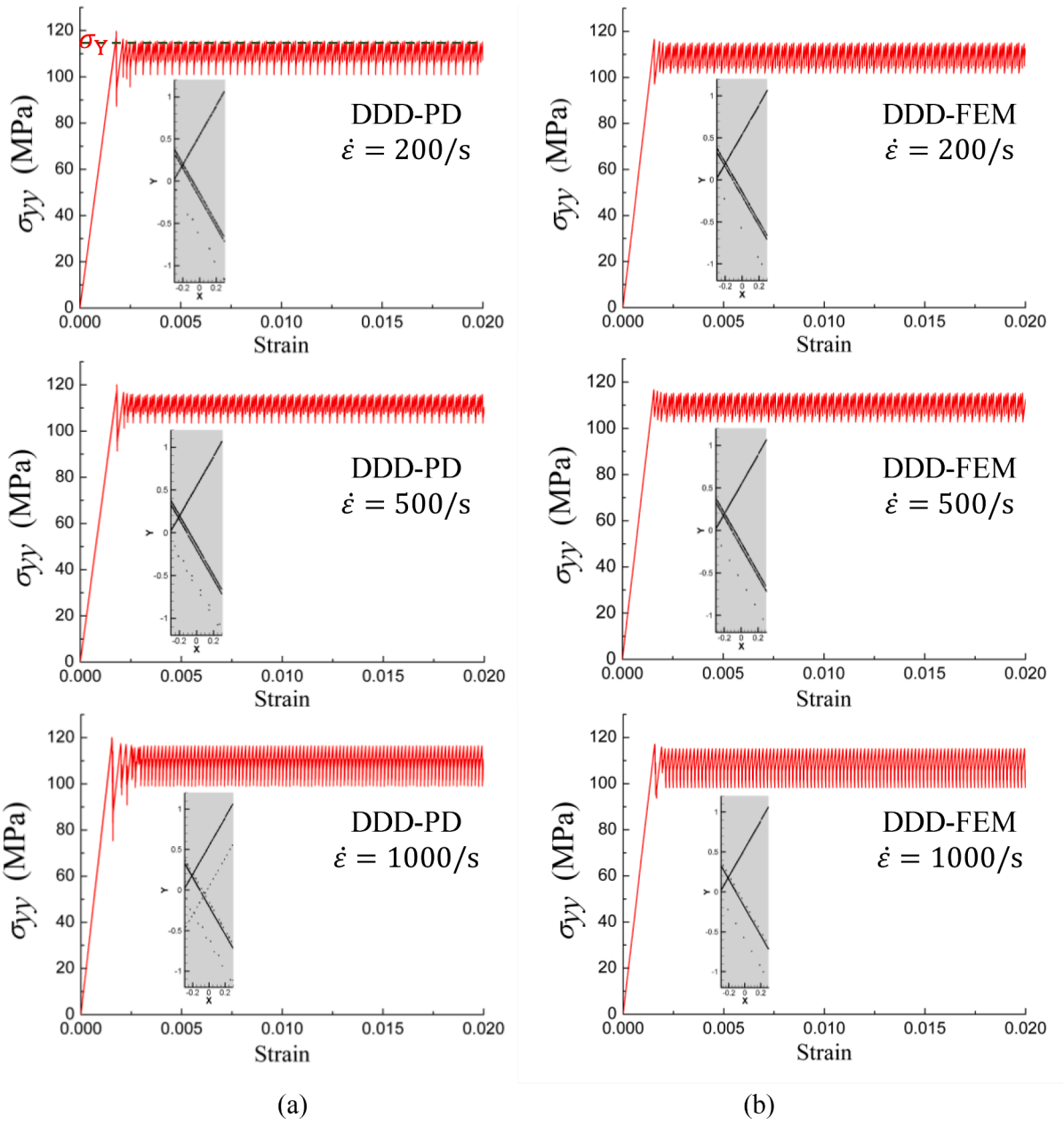


**Fig. 8.** The stress/strain curves from the (a) DDD-PD and (b) DDD-FEM models, with strain rates 200/s (upper), 500/s (middle), and 1000/s (bottom). .

plastic response. We next test the expectation that increasing the grain size leads to a decrease in the hardening rate in the plastic regime.

The stress/train curves for polycrystalline specimens with different grain sizes $d = 0.25, 0.5, 1.0, 2.0$ μm are plotted in Fig. 11. For the cases with $d = \{0.5, 1.0, 2.0\}$ μm, the horizon size is 0.4 μm. For the case with $d = 0.25$ μm, a smaller horizon size 0.2 μm is used. The stress required for the dislocations to nucleate depends on the dislocation source strength, and the direction between the slip plane and the loading direction. The stress at which the polycrystal starts to yield does not depend on the grain boundaries (see Fig. 11), while increasing the density of the grain boundary (decreasing the grain size) leads to a shorter distance for dislocation to glide, leading to a higher slope of the stress/strain curve in the strain hardening stage of deformation. The expected dependency between grain size and the plastic hardening rate is confirmed.

Moreover, the results in Fig. 11 match well those from Huang et al. (2020) calculated with the DDD-XFEM scheme. In (Huang et al., 2020), the Hall-Petch relation between grain size and the **nominal** yield stress was obtained and studied in detail. Although the stress at which the polycrystal starts to yield does not depend on the grain boundaries, the nominal yield stresses, for instance,$\sigma_{0.2}$ (at plastic

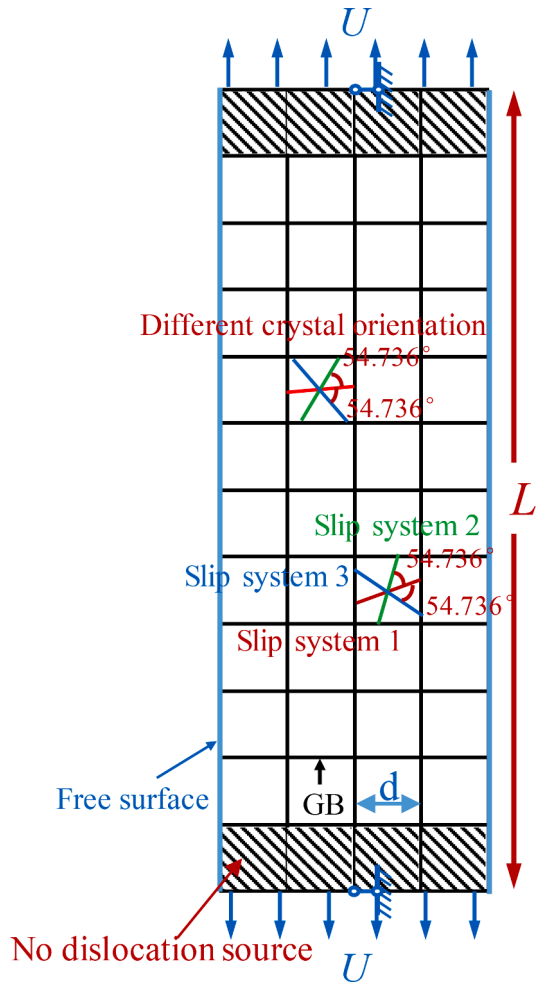


**Fig. 9.** Schematic diagram of the grains and slip systems in the polycrystalline tensile specimen.

strain$\varepsilon_p = 0.2\%$) and$\sigma_{0.4}$ (at plastic strain$\varepsilon_p = 0.4\%$), increase when decreasing the grain size. Huang et al. (2020) showed that the relationship between grain size $d$ and nominal yield stress $\sigma_{0.4}$ (at plastic strain$\varepsilon_p = 0.4\%$) is$\sigma_{0.4} = 90 + 92.4d^{-1}$. Our goal with simulating the polycrystalline sample is to compare the DDD-PD results with the corresponding DDD-XFEM ones, for model validation. A detailed analysis of the deformation mechanisms has been provided in Huang et al. (2020) and, for brevity, is not repeated here.

The stress and dislocation evolutions are also easy to obtain from the present SP DDD-PD simulations. Fig. 12 shows the contour of stress component$\sigma_{yy}$ for $d = 1.0$ μm and$\varepsilon = 0.01$. Although the uniform tensile displacement is applied, the stress field$\sigma_{yy}$ is highly uneven at the grain level. The dislocation distribution and the dislocation density distribution at$\varepsilon = 0.01$ are also provided in Fig. 12. The dislocation density is calculated by counting the dislocation number in a circular region around an arbitrary node with grid spacing as the radius, and dividing the dislocation number by the circular area around that node. The present SP DDD-PD model can, therefore, simulate dislocation-based elastoplastic behavior in polycrystals and can be helpful to understanding intrinsic plasticity mechanisms in materials.

Note that slip transfer could take place near the grain boundary, and the grain boundary morphology can play a key role in material's performance (Liu et al., 2012, 2021; Zhu et al., 2020). These are critical problems remaining to be further studied. In the current work (both Part I (Dong et al., 2022) and Part II), we present a new tool for dislocation-based plasticity and fracture analysis. We focus on validating the model and demonstrating the major advantages (handling dislocations in arbitrary domains and allowing autonomous interactions between dislocations and cracks). More realistic grain boundary morphology and interaction behavior between grain boundaries and dislocations will be studied in our follow-up research.

## 5. Indentation on a single crystal

In the last two sections, the SP DDD-PD scheme was verified for uniform tensile loading tests. In this section, we apply the method to simulate a 2D nanoindentation process on a single crystal, a classical example of non-uniform loading of a sample, to verify it for this

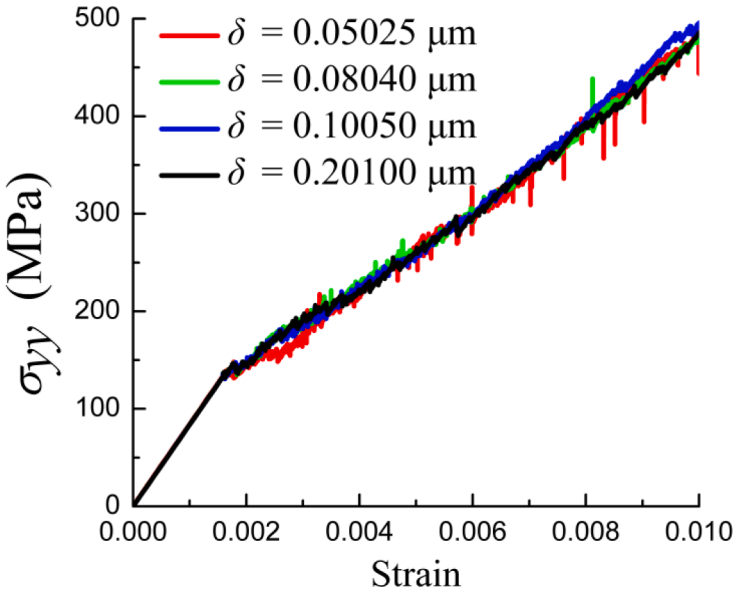


**Fig. 10.** The stress/strain curves for the polycrystalline sample (with grain size $d = 0.25$ μm) under tension for four different horizon sizes $\delta = 0.2$, 0.1, 0.08, and 0.05 μm (The number of nodes are 1904, 6144, 9164, and 21,824, respectively).

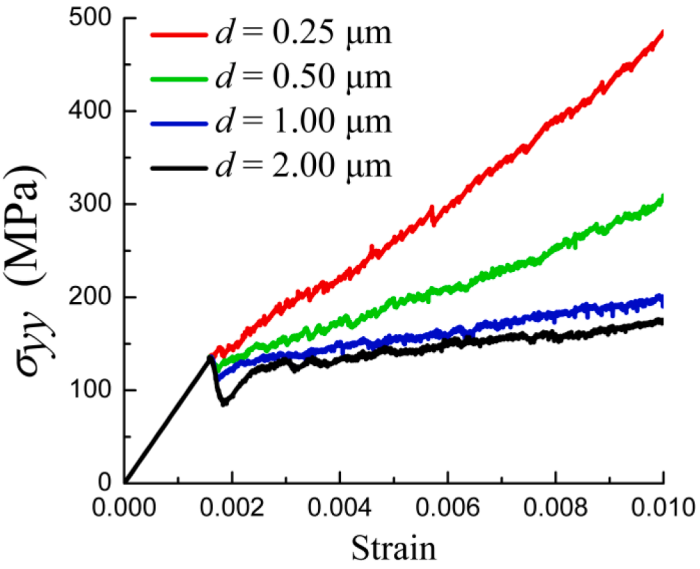


**Fig. 11.** The stress/strain curves for tensile polycrystalline specimens with grain sizes: $d = 0.25$, 0.5, 1.0, 2.0 μm, respectively. The horizon size is 0.2 μm for the cases with $d = 0.25$ μm, and the horizon size is 0.4 μm for the other cases.

more complex loading scenario. Indentation has been recognized as one of the most efficient and useful methods of determining material properties of metals (Juran et al., 2015; Zambaldi and Raabe, 2010). As a tool for mechanical characterization of materials, indentation has been widely used to determine a variety of mechanical properties of materials, such as their elastic modulus, hardening exponents, creep parameters, fracture toughness, residual stresses, etc. (Bahrami et al., 2021; Kuksenko et al., 2019).

The stress state in a specimen under indentation is complex (Karimzadeh et al., 2014). In addition, indentation is one of the few experimental techniques that can take into account both the micro and macro scale, allowing one to study material length scales from nanometer to millimeter (Cheng and Cheng, 2004) in various types of materials (Chen et al., 2013; Yang et al., 2018; Zhang et al., 2017).

Berkovich, spherical, and flat indenters are used quite frequently in experiments. Many works have been published on the simulation and understanding of dislocation evolution during the indentation process with different types of indenters (Feng et al., 2020; Lu et al., 2019; Shinde et al., 2022; Wang et al., 2019a; Xu et al., 2019). The reason we present this particular indentation case is

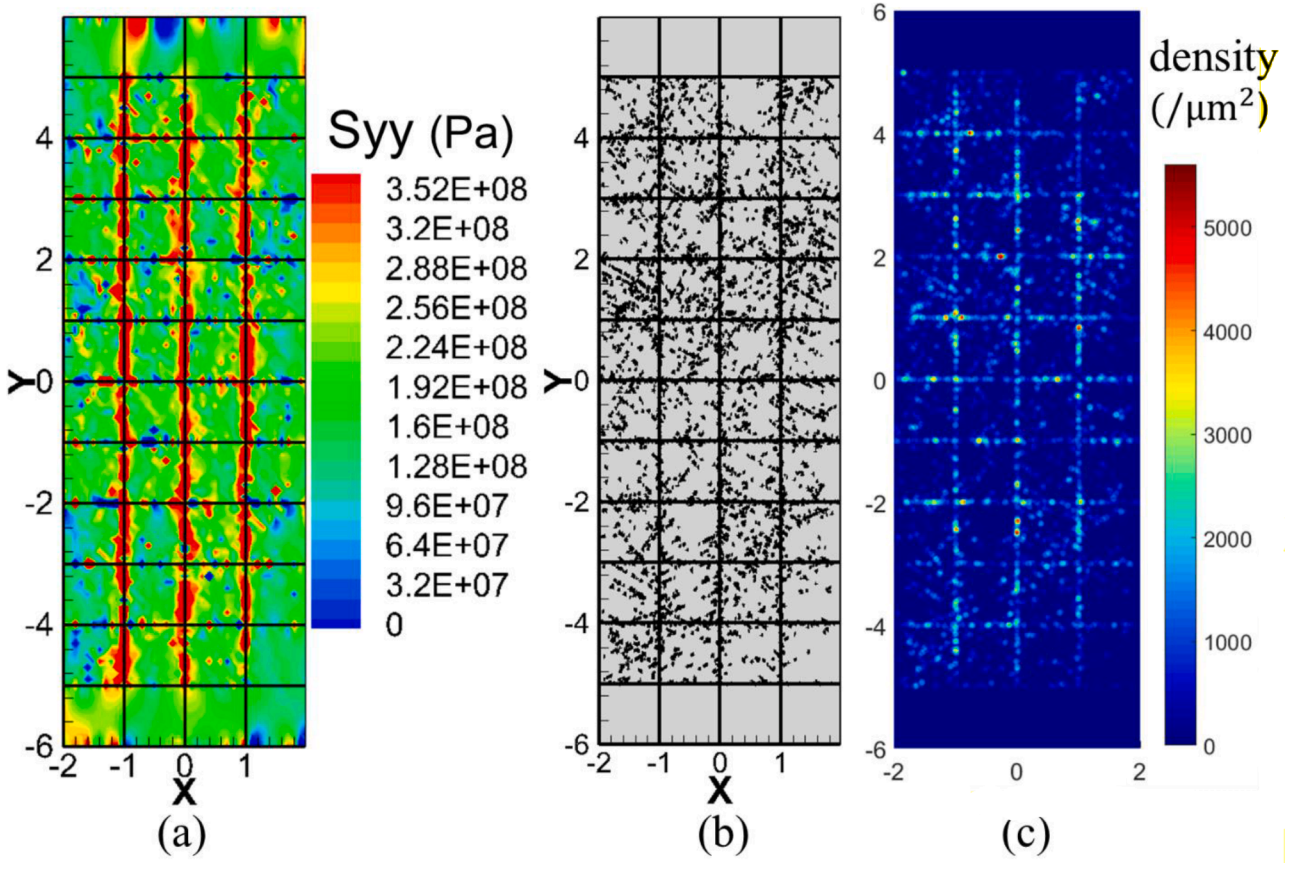


**Fig. 12.** (a) Contours of $\sigma_{yy}$ stress component, (b) corresponding dislocation distribution and (c) dislocation density at strain $\varepsilon = 0.01$, for the case with grain size $d = 1.0$ $\mu$m.

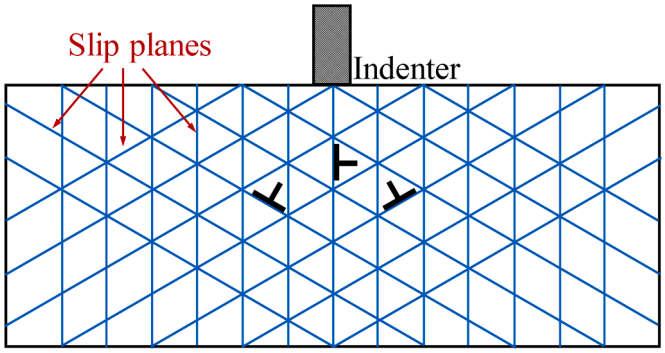


**Fig. 13.** Schematic diagram for the sample using for indentation on single-crystal aluminum.

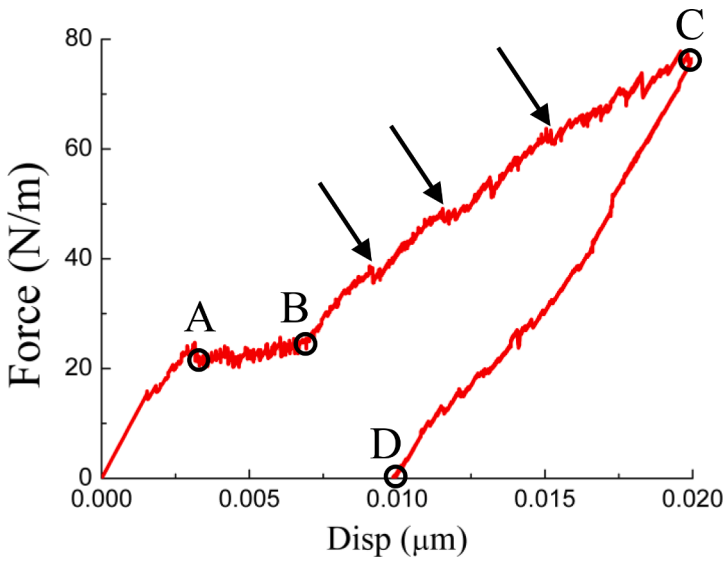


**Fig. 14.** Force-displacement curve from the SP DDD-PD simulation of indentation.

specifically to demonstrate the capability of the new model in simulating non-uniform deformations. Therefore, we select the flat indenter to observe the evolution of dislocation nucleation, gliding and "pop-in" during indentation. In addition, the flat-tip indenter can ensure a constant contact area, and the load/displacement curve is straight in the elastic stage.

The indenter is simplified into a rigid rectangles, which is illustrated in Fig. 13, although any other shapes of indenter can also be easily modelled with the present SP DDD-PD scheme. For the sake of simplicity, we assume that the contact surface between the specimen and the indenter is completely smooth, and ignore the influence of any surface roughness that may be present in an experimental sample.

As shown in Fig. 13, the indenter width is 0.28 μm. The width of the specimen is 5 μm, and the height is 2 μm. We use a horizon size $\delta = 0.0804$ μm (node spacing 0.02 μm). The size-dependency of indentation is greatly affected by the density of dislocation obstacles and sources (Campilho et al., 2011; Zhang et al., 2014). For simplicity, no obstacles are set in the indentation simulation. To make the specimen nucleate enough dislocations during compression consistent with reality, a larger dislocation source density $\rho = 500/\mu m^2$ is considered here. Three slip systems are input with intersection angles between the slip systems and the positive x-axis of 30°, 90°, 150°, respectively (see Fig. 13). Other parameters, such as Young's modulus $E$, Poisson's ratio $\nu$ and DDD parameters, are set the same as those given in Sections 3 and 4. The displacement component $u_x$ on the bottom boundary and component $u_y$ for the center point on the bottom boundary are kept fixed as 0. Other boundaries are set as free surfaces. The moving direction of the indenter is from top to bottom, with a speed of $500\mu m/s$.

The indenter is unloaded and returned to its original position after moving downward 0.02 μm. The force-displacement curve for the whole process, including loading and unloading, is shown in Fig. 14, which is quantitatively consistent with the theoretical solution described in (Hu et al., 2015). It can be seen from the force-displacement curve that there is an obvious yield in the early stage of loading (from A to B in Fig. 14), namely "pop-in", which is believed to be caused by uniform nucleation of dislocations under the indenter. This phenomenon has also been noticed in some experiments and simulations (Durst et al., 2006; Shim et al., 2008; Zhou et al., 2020). In addition, staircase yield (arrowed locations in Fig. 14) also occurs in the later loading stages. This phenomenon may be

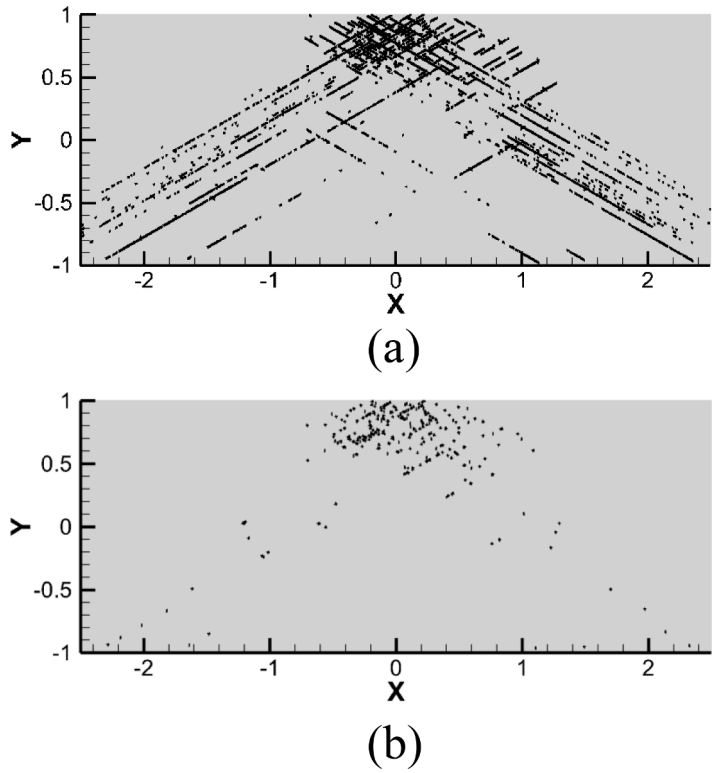


**Fig. 15.** (a) The traces of all dislocations during the indentation process. (b) The traces of dislocations in the specimen at the time when the indenter is at the maximum depth. Units on axes are μm.

related to the indenter size and the loading rate (Cordill et al., 2009).

As shown in Fig. 14, at the initial stage, the deformation is purely elastic and no dislocation nucleates. The load-displacement curve is linear, matching with the analytical solution of Hu et al. (2015). At the first plastic stage (when the material starts to yield), the number of dislocations in the material is small. As a result, the nucleated dislocations can glide out from the free surface soon after their nucleation. Therefore, the force-displacement curve is relatively flat (the first "pop-in" plateau from A to B in Fig. 14). As dislocation interactions between different slip systems take place, more and more dislocations remain in the material. The chance for dislocations gliding away at the surface becomes limited, leading to a stiffening effect and a steeper load/displacement behavior. In the unloading stage (from C to D in Fig. 14), the force decreases gradually.

During the simulated nanoindentation process, we record all traces of dislocations, and these are shown in Fig. 15a. In addition, the dislocation distribution produced by the indenter impressed at its maximum depth is provided in Fig. 15b. Dislocations are concentrated, as expected, in the region just below the contact between the indenter and the sample (Javaid et al., 2017; Pharr et al., 2010).

In the previous sections, we have verified SP DDD-PD model's ability to simulate dislocation-based elastoplastic deformations and track dislocations' evolution, under uniform and non-uniform loadings. In the next section, we will investigate the use of the new model for elastoplastic fracture problems. We shall see how initiation and propagation of both dislocations and cracks can be autonomously captured by the SP DDD-PD scheme.

## 6. Mode I elastoplastic fracture

In this section, the DDD-PD model is employed to study Mode I elastoplastic fracture in a single crystal, by allowing failure of PD bonds. Specimens with different sizes will be considered to study the size effect on the elastoplastic fracture behavior. We also analyze the dependence of fracture results on the input fracture toughness of the material, by using different critical bond strains (bond strain beyond which the bond sustains zero force) and calculating the corresponding strain-to-failure for the specimen.

### *6.1. Damage model*

In this section, we extend the SP DDD-PD scheme to allow simulation of damage evolution. In the SP DDD-PD model, the bond strain is composed of elastic and plastic parts. The plastic bond strain part is induced by the dislocations and slip planes crossing the PD bonds. This strain is assumed to not directly contribute to damage and fracture, but only to the permanent plastic deformation. The initiation, growth, and coalescence of micro-voids induced by the dislocations' evolution are treated as plastic deformation in the

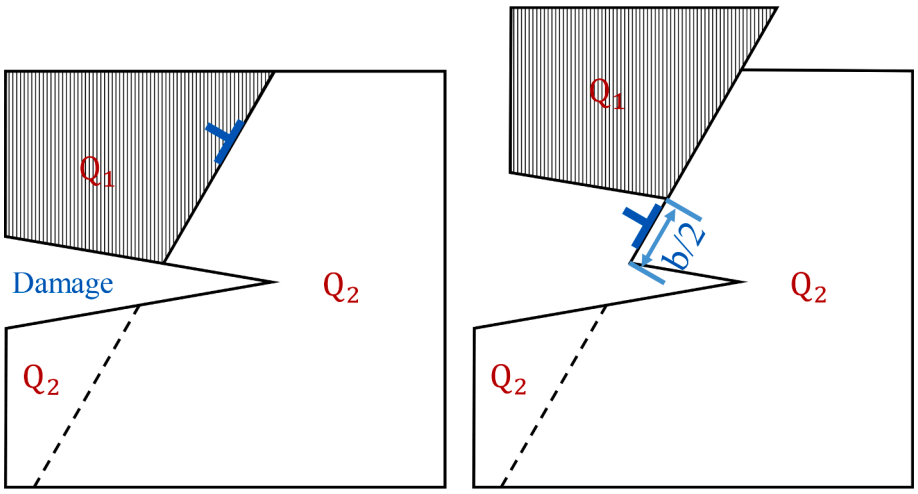


**Fig. 16.** Displacement produced by a dislocation gliding out from the upper surface of a crack in a single crystal.

model. Here we assume that damage can only be induced by elastic bond strain exceeding a critical value, i.e., the critical bond strain. In Part I of this work (Dong et al., 2022), the PD solver for elastic behavior has been briefly reviewed. A linear elastic model with brittle damage, the original Prototype Micro-Brittle (PMB) material model, is adopted here to describe damage.

In the PMB model, the local damage at a material point ($\boldsymbol{x}$) at time $t$ is therefore expressed by a damage index$\varphi$, defined as

$$\varphi(\boldsymbol{x},t)=1-\frac{\int_H \mu(\mathrm{x},t,\boldsymbol{\xi})\mathrm{d}V}{\int_H \mathrm{d}V} \tag{5}$$

where$\boldsymbol{\xi}$ is the relative position of a PD bond, $H$ is the horizon of material point $\boldsymbol{x}$, and$\mu$ is a scalar function that characterizes whether the bond is broken.

$$\mu(t,\boldsymbol{\xi})=\begin{cases}1 & if\ s_{\mathrm{e}}\le s_0\\ 0 & otherwise\end{cases} \tag{6}$$

where$s_{\mathrm{e}}$ is the elastic part of the bond strain, and$s_0$ is the critical bond strain. For brittle fracture, the critical bond strain is usually calibrated to the critical fracture energy (material fracture toughness). When the damage index at a point is greater than 0.5 (Silling and Askari, 2014) (in the discrete form, this critical value depends on the horizon factor $m$), then a crack is formed. In this work, because we currently do not have a theoretical connection between a material's fracture toughness and the critical PD bond strain for our new model (linear elastic, brittle fracture, plus dislocations), we select some arbitrary values for the critical bond strain. The computational tests below will, however, show a linear dependence between the strain-to-failure and the critical bond strain values.

Once damage is introduced, it becomes necessary to consider the newly formed boundaries and their effect on dislocation evolutions. In Section 3, it has been demonstrated that when a dislocation glides out from the boundary, it no longer produces stress field in the model, instead leading to a permanent displacement, via a step on the surface (see Fig. 4). In the models discussed in Sections 3–5 (no damage present), the dislocation could only glide out from the initial boundaries. Because the domain is simply connected, it was easy to deal with displacements induced by dislocations. When damage is present, the dislocations could glide out from any damage surface. The original continuous slip plane could be separated by newly formed damages or cracks (see Fig. 16). Therefore, in the simulations with damage, once a slip plane intersects a damage region (e.g. a crack surface), we relabel the slip plane into two individual slip planes with new starting and ending positions. As shown in Fig. 16, considering a finite model with damage placed in the middle and an edge dislocation located in the undamaged part of the model, the dislocation slip plane is truncated due to damage. In this case, the structure, like the one shown in Fig. 4, can also be divided into two regions ($Q_1$ and$Q_2$, in Fig. 16). As shown in Fig. 16, a relative rigid displacement between these two regions is induced after the dislocation glides out from the surface. The computational flow to implement the relative rigid displacement induced by a dislocation gliding out from the crack surface is shown in Appendix B.

### 6.2. Size effect

In this subsection, we apply the DDD-PD model to study Mode I elastoplastic fracture in a single crystal. The numerical parameters and boundary conditions are shown in Fig. 17. Square specimens with sides $L$ of 2.5, 4.3, and 6.0 μm are considered. A pre-crack is set in all specimens, and the ratios of pre-crack length to side length $L$ are fixed at 0.3. Young's modulus $E$, Poisson's ratio$\nu$ and DDD parameters are the same as those in Section 3 for single-crystal aluminum. We set the critical bond strain to 0.009. Three slip systems intersecting with the x-axis positive direction at angles of 0°, 60°, 120° are assigned. The distance between neighboring slip planes of the same slip system is 25 nm. In the PD model, the horizon size$\delta = 0.0804$ μm.

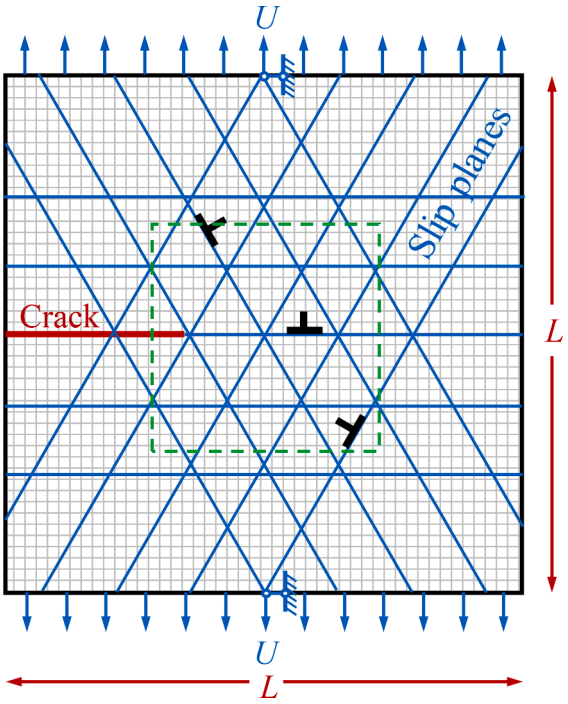


**Fig. 17.** Slip planes setting of a model with pre-crack. The green dash square at the center represents the path for *J*-integral (see Appendix C). The square side length are 2 μm.

A displacement boundary condition with a strain rate of$\dot{\varepsilon} = 1000/\mathrm{s}$ is applied in the Y direction of the upper and lower boundary of the model, the left and right boundaries are free boundaries, and the transverse coordinates of the upper and lower center points of the model are fixed.

The pre-defined crack shown in Fig. 17 is applied to mimic the pre-crack set in the experiments. With a pre-crack, one is assured that the crack will grow from the tip of the pre-crack. Other methods (Curtin et al., 2010; Liang et al., 2019) require a pre-defined path, usually set as straight line, for the growing crack (which will grow from the tip of the pre-crack). The DDD-PD model does not require a preset path for the growing crack. PD models, by embedding simple bond-damage rules, are general enough to be able to reproduce, autonomously, complex evolution paths for damage or crack propagation without any explicit tracking of interfaces/cracks/boundaries.

Fig. 18 shows the final damage map for the specimen with a side length of 4.3 μm with dislocations and without dislocations, respectively. Mode I brittle cracks (in a homogeneous material) are generally straight, unless crack branching occurs. The final crack path shown in Fig. 18a is not straight. The reason is that dislocations nucleated from a random distribution of dislocation sources affect the stress field and thus the crack propagation path. Once the crack propagates out from the rectangle-labeled region in Fig. 18a, the crack enters into the brittle fracture phase and appears as a straight line. The tortuous geometry of the elastoplastic crack path found by our model matches well with experimentally-observed cracks formed in single-crystal materials. For instance, (Creuziger et al., 2008; Kalácska et al., 2020; Sumigawa et al., 2018) showed that tension-induced fracture surfaces in single crystals such as copper, tungsten and NiAl are not straight or zig-zaged, but smooth and undulating, indicating that dislocations are critical, not crystal anisotropy. The departure from a straight crack is not captured in the other DDD simulations of Mode I elastoplastic fracture in a single crystal. To simulate elastoplastic fracture by using the traditional DDD methods, the fracture propagation paths need to be preset, usually, as straight lines (Liang et al., 2019), and a cohesive zone implemented. With the present SP DDD-PD model, autonomous crack growth can be easily simulated, and the crack path can take any arbitrary shape (even become a "diffuse", or distributed damage region, instead of a "path"), depending on the conditions present in the system. This enables simulating the interaction between dislocations and cracks with high fidelity.

Note that the asymmetry of the crack path (see Fig. 18a) is induced by the higher density of active glides on one side, ahead of the crack tip, than the other. The gliding of dislocations "attracts" the crack path towards that region. The original source of break of symmetry is the random distribution of locations and strength of dislocations used here. See Movie 2 in Supplementary Materials.

Fig. 19 shows the stress-strain curves during the whole loading process (from the beginning to full sample splitting) for all three geometry cases. The plotted stress is computed by the average of all node stresses on the top side. For the case with $L = 4.3$ μm, several snapshots of damage maps are given as insets in Fig. 19. Damage evolution and crack propagation are similar for all three cases considered. Because of this, only damage maps for the case with a medium side length are shown. At an applied strain of 0.000863, dislocations start to nucleate near the crack tip. As the loading increases, more and more dislocations nucleate. When the applied strain reaches 0.0015, peridynamic bonds start to break at the crack tip. At this moment, the crack propagation rate is low. The crack grows

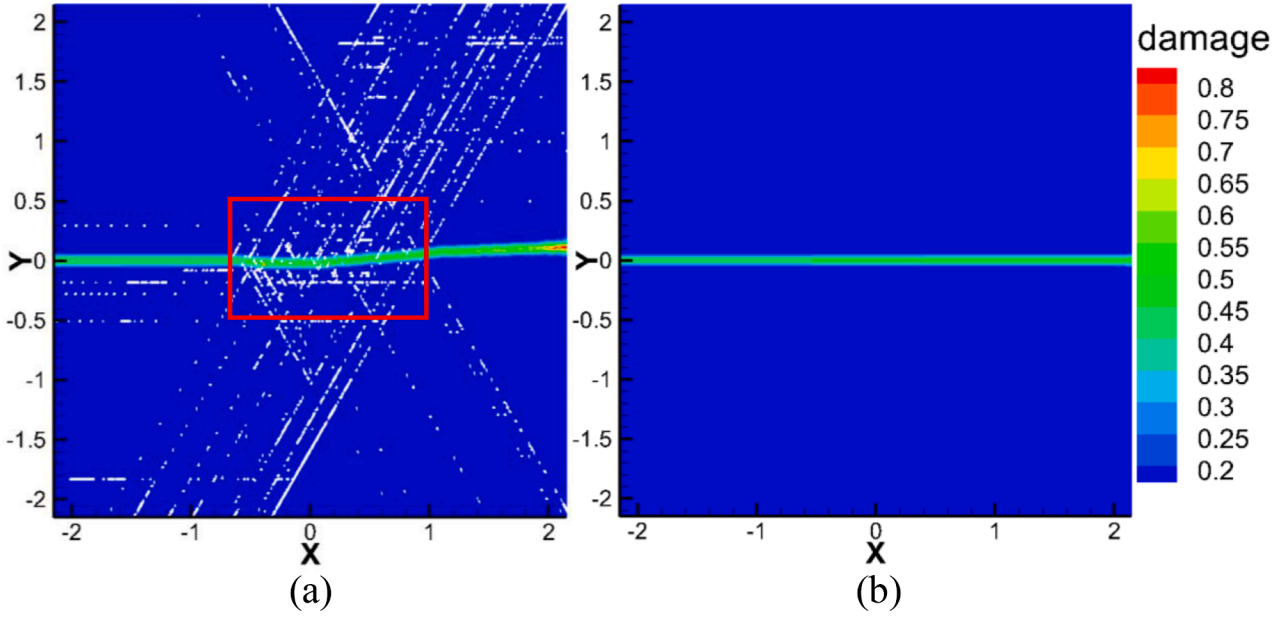


**Fig. 18.** The final damage map from Mode I fracture in a pre-cracked specimen with side length $L = 4.3$ μm (a) with dislocations and (b) without dislocations (brittle fracture), respectively. In (a), the superposed white dots indicating the traces of all dislocations during the fracture process, and the tip of the pre-crack is at the middle of the left side of the Red Box. The departure from a straight crack is most pronounced in the region inside the Red Box. Units on the axes are μm.

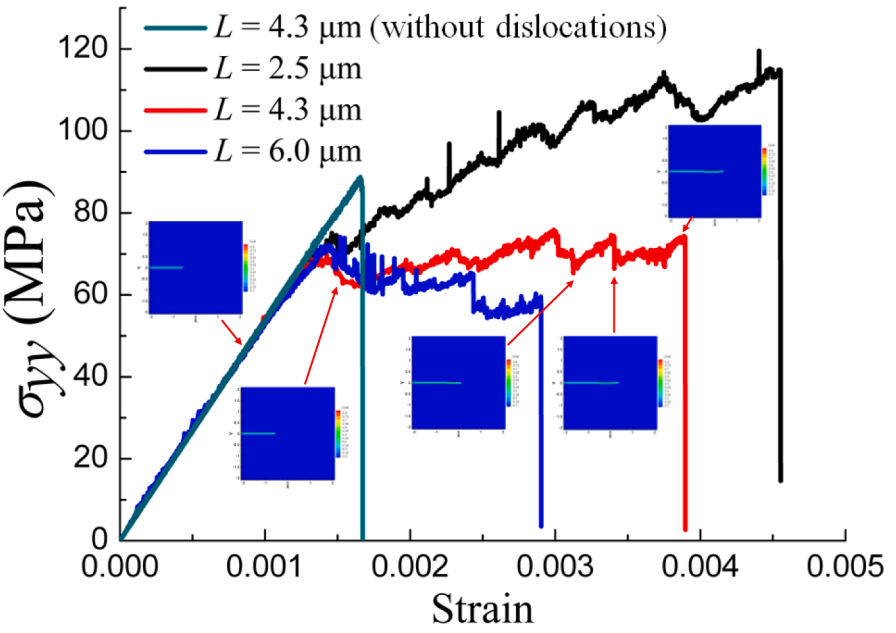


**Fig. 19.** The stress/strain curves from Mode I fracture of pre-cracked square specimens of different sizes. The insets are snapshots of damage maps for the specimen with $L = 4.3$ μm and taken at strains corresponding to the locations pointed to by the arrows, respectively.

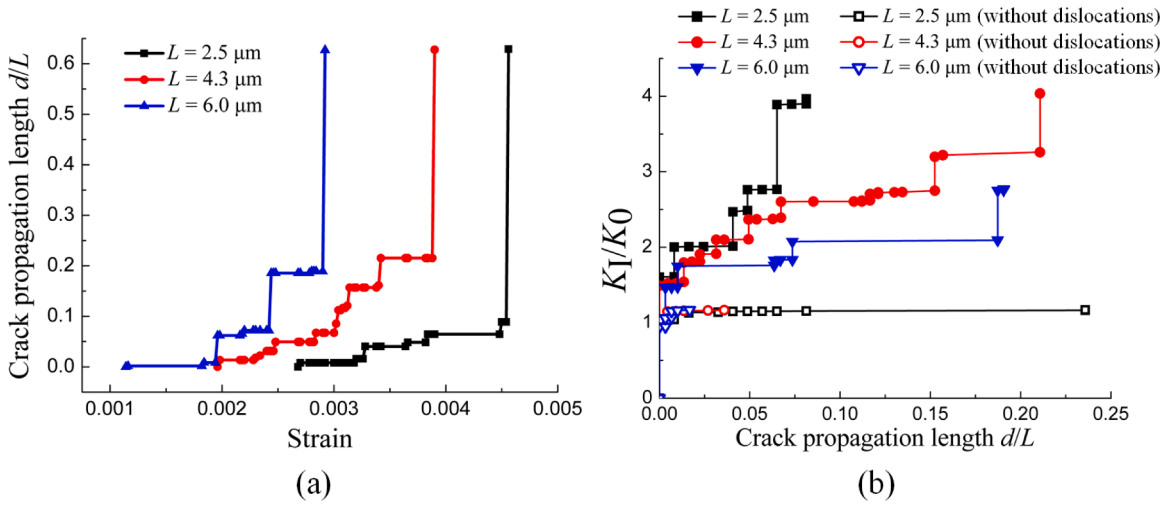


**Fig. 20.** (a) Normalized crack length versus strain for the different size specimens. (b) The normalized stress intensity factor $K_I/K_0$ computed by the DDD-PD model vs. the obtained crack extension for the different samples, with or without considering dislocations.

faster around time $t = 2820$ ns when strain approaches 0.00282. When time $t = 3900$ ns and strain reaches 0.0039, the stable ductile fracture transitions to brittle fracture, and the sample breaks instantly.

Fig. 20a shows the normalized crack length as a function of the applied strain, for the three specimen sizes. The figure reveals that under the same tensile strain rate, the larger the crystal specimen size is, the earlier the cracking occurs. After fracture initiates, there is a stable crack growth regime, followed by a transition to sudden, unstable crack growth. By using linear curve fits over the stable crack growth stage, we extract crack speeds of 0.11383, 0.64358, and 1.13085 m/s for specimens with $L = 2.5$, 4.3, and 6.0 μm, respectively. This indicates that in the stable crack growth stage, the smaller the single crystalline specimen size is, the lower the crack propagation speed and the higher the tensile fracture resistance are Fig. 20b shows the evolution of the normalized stress intensity factor (SIF) for different cases (see Appendix C for the way to calculate SIF in PD). In Fig. 20b, the critical SIF is $K_0 = \sqrt{\frac{G_0 E}{(1-\nu^2)}}$, where $G_0$ is the material's fracture energy. Notice that the trends are very similar to what (Cleveringa et al., 2000) also found, while using imposed values of $K_I$ and only computing the corresponding crack advancement in a model with a preset crack-path. In our model, the crack growth is autonomous, and found to follow towards the regions of higher density of active gliding dislocations.

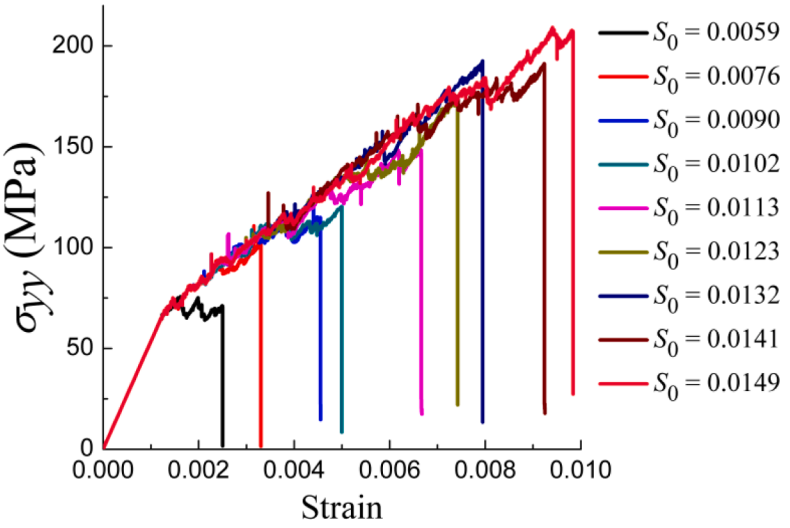


**Fig. 21.** The stress/strain curves for different critical PD bond strains for the model of size $L = 2.5$ μm.

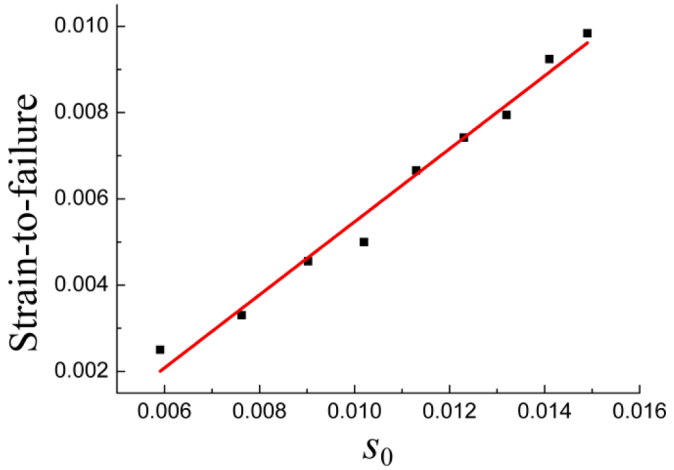


**Fig. 22.** The linear curve-fit for different critical bond strains $s_0$ and the PD-computed corresponding strain-to-failure.

For the specimen with a smaller size, the number of dislocations is fewer, leading to an effective higher stress to initiate the dislocations and a larger slope on the post-yield stress-strain curve (see Fig. 19). The dislocations moving distance from the nucleation sites to the boundary are statistically shorter for the smaller specimen, making it easier to dissipate energy via dislocation-induced plasticity. Therefore, both the toughness (i.e., the area surrounded by the stress/strain curve and the strain-axis, in Fig. 19) and the strain-to-failure increase with decreasing the sample size, indicating that the ability to resist damage is enhanced with a decrease of the sample size.

Movies 1–6 show how the sample size affects the behavior: given the proximity of the imposed boundary conditions (fixed values for vertical displacements, that grow at a constant rate in time) to the crack tip (the main "defect" in the sample), we notice a higher density of pinned dislocations in the smaller sample than in the larger ones. In the larger samples, the constraint imposed by the boundary conditions is sufficiently far away from the high stress-intensity region to allow for less dislocations nucleation away from the crack tip. This explains the ductile fracture part of the observed behavior. Note that some dislocations are nucleated, as expected, from the constraints on the top and bottom boundaries, likely being influenced by the slight PD surface effect still present there. The reason for the transition from ductile to brittle fracture is the presence of the free boundary on the right. If the crystal analyzed here were part of a polycrystal, this is could still happen in two possible scenarios: (1) if the growing crack approaches an existing microcrack that sits at a grain boundary, or (2) if dislocations pile up at a grain boundary, leading to increased stress-intensity and eventually to a brittle, more catastrophic failure.

The above results showed that the SP DDD-PD scheme can simulate elastoplastic fracture problems: interactions between dislocation evolution and autonomous crack propagation are obtained by combining a brittle fracture model with dislocation-based plasticity, without the need of a cohesive zone model. In the PD module, the damage is brittle. For linear elastic and brittle

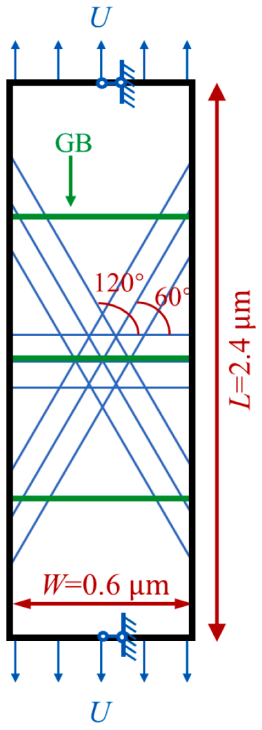


**Fig. 23.** Loading conditions and slip planes distribution in the uniaxial tension test of aluminum crystal with three rigid grain boundaries.

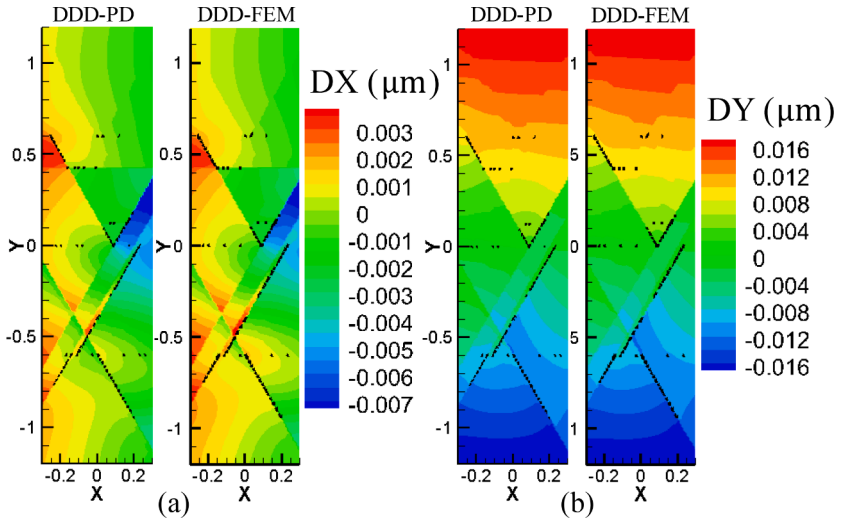


**Fig. 24.** Horizontal (a) and vertical displacements (b) at applied vertical strain $\varepsilon = 1.5\%$, obtained from the DDD-PD and DDD-FEM models for the crystal with three rigid grain boundaries. Strain rate $\dot{\varepsilon} = 500/\text{s}$.

fracture behavior, the critical bond strain has a square root dependence on the critical fracture energy. However, in elastoplastic fracture, the total energy dissipated contains the energy consumed by plastic deformation, induced by dislocation motion/evolution. An analytical formulation for the relationship between the critical bond strain and the critical fracture energy in elastoplastic fracture is the subject of future studies. In the next section, we study this dependence numerically, using the PD model we introduced and setting different critical bond strains (beyond which the PD bonds break) and computing the corresponding strain-to-failure.

### *6.3. The dependence between strain-to-failure and critical bond strain*

By using the same numerical parameters and boundary conditions as above, we employed the SP DDD-PD scheme to simulate

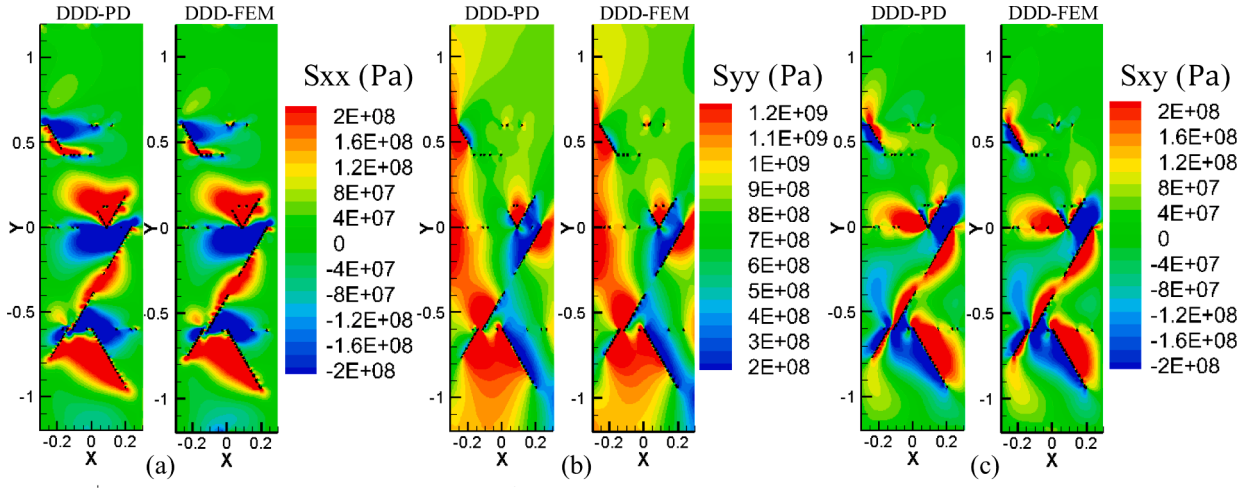


**Fig. 25.** Normal (in (a) and (b)) and shear (in (c)) stress componenets at imposed vertical strain $\varepsilon = 1.5\%$, obtained from the DDD-PD and DDD-FEM models for the crystal with three rigid grain boundaries. Strain rate $\dot{\varepsilon} = 500/s$.

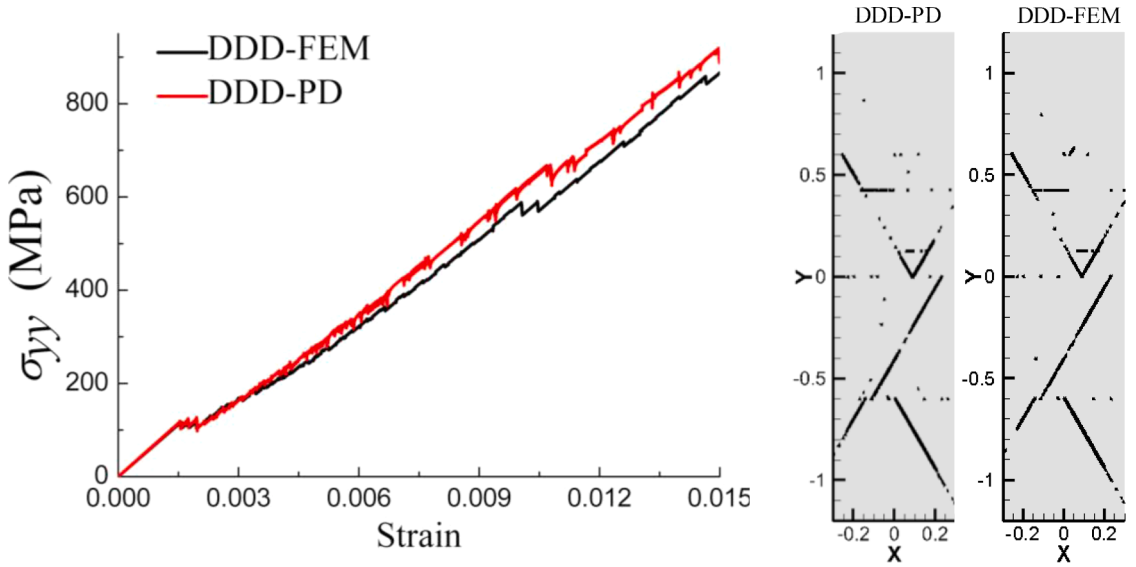


**Fig. 26.** The stress/strain curves and the traces of all dislocations during uniaxial tension for the crystal with three rigid boundaries.

Mode-I fracture of the specimen with side length $L = 2.5$ μm for different critical bond strains$s_0$ (see Eq. (6)), to observe the influence of this parameter (related to material's fracture energy) on the failure response. Fig. 21 shows the stress-strain curves for cases with different critical bond strains between 0.0059 and 0.0149. When the critical bond strain is smallest (0.0059), the stress-strain curve post-yield does not show any hardening, in contrast with the curves from the other values of$s_0$. Those curves all have a similar hardening rate. We suspect this happens because for the smallest$s_0$ value, the failure behavior is approaching quasi-brittle one. With larger$s_0$, more dislocations have a chance to initiate, leading to the noticeable hardening behavior before brittle failure.

The computed strain-to-failure values corresponding to each of the critical bond strains used above are recorded and presented in Fig. 22. A linear relationship between the strain-to-failure and the critical bond strain is revealed. Although an analytical relationship between the critical bond strain and the material's fracture toughness (or critical fracture energy) is not yet available, one could use this numerically-obtained linear relationship to calibrate the SP DDD-PD fracture model to experimental data. For example, with only two runs of the SP DDD-PD model (for a sample size on which experiments are performed) using two different$s_0$ values, one can determine the linear dependency, then using the experimental strain-to-failure data, the corresponding$s_0$ that needs to be used in the model is found.

Although extending the present 2D model to 3D is straightforward, the main difficulty for the 3D simulation is the much higher computational cost. As we commented in Part I of this work (Dong et al., 2022), coupling PD (with the meshfree discretization method), used where damage/cracking happens, with a local model (discretized with FEM, for example) used outside of areas (see

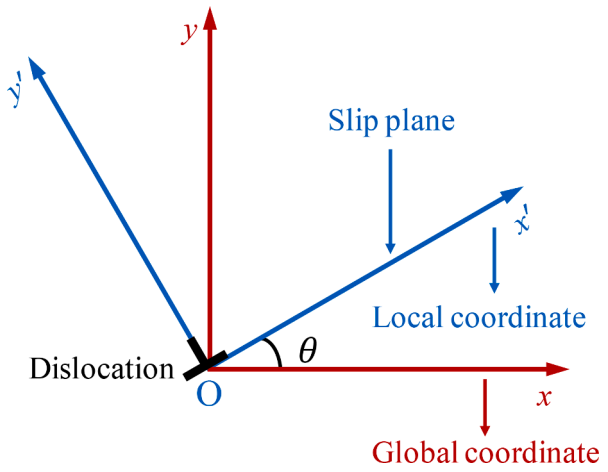


**Fig. 27.** A local coordinate system with its origin at a dislocation core.

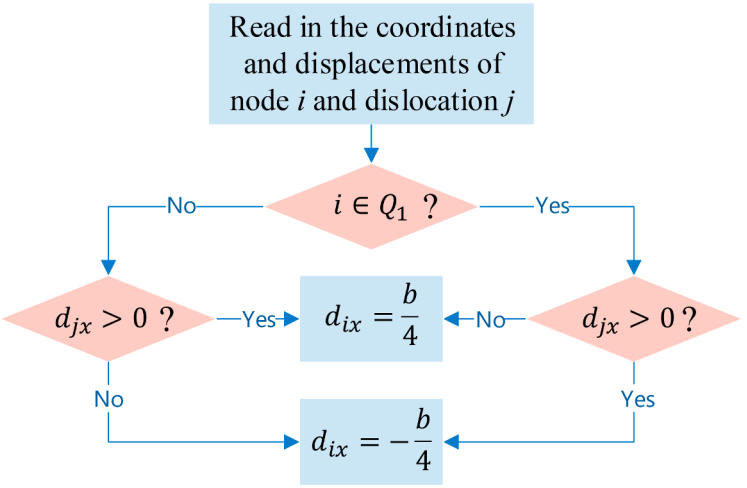


**Fig. 28.** Algorithm for implementing the permanent displacements at nodes affected by dislocations gliding out from a crack surface.

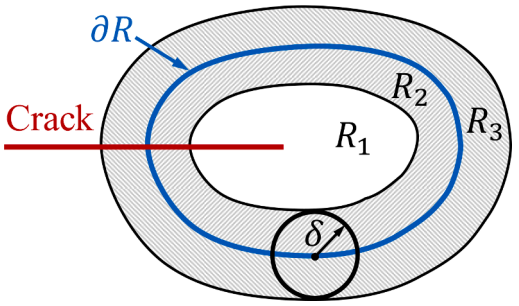


**Fig. 29.** Scheme of the path for PD J-integral calculation.

Galvanetto et al. 2016, Pagani and Carrera 2020) where damage takes place, can lead to numerical approaches that combine the advantages of the local and nonlocal models while reducing their respective disadvantages: FEM solvers for local models are fast, but cannot always correctly represent fracture/damage evolution, while PD models with meshfree discretization get the correct failure mechanisms but are computationally very expensive. Another promising way is the convolution-based method (Jafarzadeh et al., 2020, 2022), which can reduce the computational complexity of PD models from $O(N^2)$ to $O(N\log_2 N)$, with $N$ being the total number of discretization nodes. We plan to explore solving 3D DDD-PD models in the future using these new techniques.

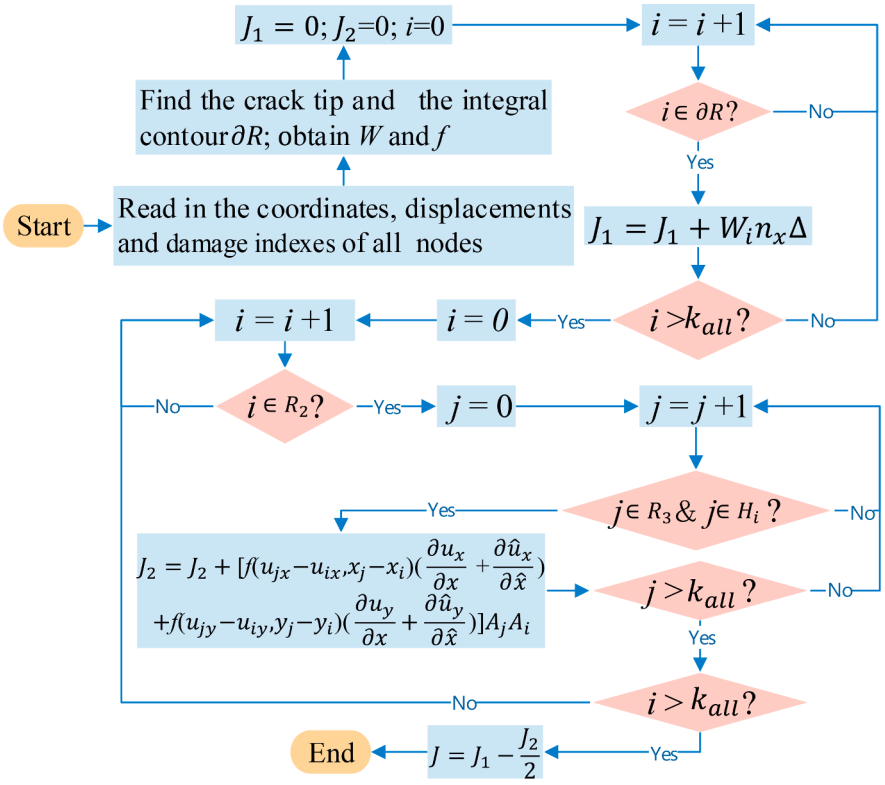


**Fig. 30.** Computations flow for the PD J-integral.

## 7. Conclusions

In the first part of this work (Dong et al., 2022), we introduced an SP version of DDD-PD coupling scheme. The scheme has been verified on several BVPs with stationary dislocations: simply-supported single crystal with single edge dislocation, multiple edge dislocations, dislocation emitted from a crack tip, and interaction between dislocation and void.

In the present second part of this work, we extended the SP DDD-PD scheme to consider nucleation, glide, annihilation, and motion of dislocations. Moreover, we enhanced the model to include bond-breaking, allowing us to consider problems with dislocations and growing cracks. The SP DDD-PD framework includes two major parts: the DDD and the PD modules. The DDD part models the dislocation evolution, which is transferred to the PD module. The PD module is employed to satisfy the boundary conditions. The stress field obtained by PD module is transferred back to the DDD module, driving the evolution of dislocations.

Using the SP DDD-PD scheme, we studied the uniaxial tension of single crystal and polycrystalline aluminum. Results were compared with those obtained from SP DDD-FEM (the case with single-crystal specimen) and DDD-XFEM (the case with polycrystal aluminum) schemes, verifying the SP DDD-PD scheme for corresponding plasticity problems. The famous Hall-Petch relation between the grain size and the nominal yield stress in a polycrystal has been captured successfully. Elastoplastic indentation was also simulated with the present SP DDD-PD scheme, and the well-known "pop-in" behavior was captured correctly.

We showed that the present SP DDD-PD scheme can simulate elastoplastic fracture by considering the autonomous interactions between dislocations and crack growth. For obtaining these results, neither a preset cracking path nor a cohesive zone model is needed. Using the new model, Mode I elastoplastic fracture in a single crystal is simulated. We noticed that the crack path is “attracted” towards regions of high density of gliding dislocations, leading to an undulating crack paths, as observed in experiments but never replicated by continuum-level computational models before. Tests on different sample sizes showed how the proximity of constraints to the crack tip can lead to plastic hardening. Ductile-to-brittle transition can happen naturally in the model when the crack, under Mode I displacement-controlled loading, approaches a free edge.The numerical results found a linear relationship between the strain-to-failure and the critical bond strain. This could be used in the future to calibrate the DDD-PD fracture model to experimental data.

## CRediT authorship contribution statement

**Wenbo Dong:** Software, Formal analysis, Writing – original draft. **Hengjie Liu:** Software, Formal analysis, Writing – original draft. **Juan Du:** Investigation, Writing – review & editing. **Xu Zhang:** Investigation, Writing – review & editing. **Minsheng Huang:** Investigation, Funding acquisition, Writing – review & editing. **Zhenhuan Li:** Investigation, Writing – review & editing. **Ziguang Chen:** Conceptualization, Supervision, Software, Formal analysis, Funding acquisition, Writing – original draft, Writing – review &

editing. **Florin Bobaru:** Investigation, Formal analysis, Writing – review & editing.

## Declaration of Competing Interest

The authors declare that they have no known competing financial interests or personal relationships that could have appeared to influence the work reported in this paper.

## Data availability

No data was used for the research described in the article.

## Acknowledgments

This work was supported by the Natural Science Foundation of China (No. 11802098 and 11822204) and the Fundamental Research Funds for the Central Universities (No. 2021GCRC021). The work of F.B was supported in part by the National Science Foundation under CMMI CDS&E award No. 1953346. We would like to thank the anonymous reviewers for the very insightful and valuable comments and suggestions that have led to a much improved version of our paper.

## Supplementary materials

Supplementary material associated with this article can be found, in the online version, at doi:10.1016/j.ijplas.2022.103462.

## Appendix A. Uniaxial tension of a crystal with three rigid boundaries

In this appendix, we consider the same problem shown in Fig. 2, but with three rigid boundaries in the crystal (see Fig. 23). Figs. 24–26 show the numerical results for displacement and stress fields at the applied vertical strain $\varepsilon = 1.5\%$, and the stress/strain curves obtained with the SP DDD-PD and the SP DDD-FEM schemes.

## Appendix B. An algorithm to implement the relative rigid displacements at nodes induced by dislocations gliding out from a crack surface

When a dislocation *j* glides out from a crack surface (see Fig. 16), rotate the global coordinate (*Oxy*) of the dislocation and all nodes to a local coordinate system (*Ox'y'*, the dislocation coordinates are taken as the origin, and the slip plane is the *x'*-axis, as shown in Fig. 27). Fig. 28 shows the computational flow to obtain the relative rigid displacement$(d_{ix}, d_{iy})$ of node *i* in the local coordinate system due to the dislocation *j*. The global displacement$(D_{ix},\ D_{iy})$ of node *i* due to the dislocation *j* can be calculated from:$D_{ix} = d_{ix}\cos\theta$ and$D_{iy} = d_{ix}\sin\theta$, where$\theta$ is the angle between the slip plane and the *x*-axis (see Fig. 28). Note that the final displacements need to be multiplied by the sign of the dislocation.

## Appendix C. Calculation of the stress intensity factor

The use of the J integral inside the sample (where dislocations are being nucleated and gliding) is to be taken here only as an approximation. Since we are not modeling the elastic region far from the process zone, like it is done in, for example, Cleveringa et al. (2000), where a given *K*-field is imposed in the model, the only option is to try contours like the ones shown in Fig. 17 and compute *K* based on the *J*-integral value. While changing the contour will likely change the *J*-value, we think that the overall trends seen from the results shown in Fig. 20b are not affected in a significant way.

The peridynamic J-integral formula in 2D is (see Hu et al. 2012):

$$J_{\text{peri}} = \oint_{\partial R} W n_x \mathrm{d}S - \frac{1}{2}\oint_{R_2}\oint_{R_3} \mathbf{f}(\widehat{\boldsymbol{u}} - \boldsymbol{u}, \widehat{\mathbf{x}} - \mathbf{x}) \cdot \left(\frac{\partial \widehat{\mathbf{u}}}{\partial \mathrm{x}} + \frac{\partial \mathbf{u}}{\partial \mathrm{x}}\right) \mathrm{d}A_{\widehat{\mathbf{x}}} \mathrm{d}A_{\mathbf{x}}$$

One-point Gaussian quadrature and uniform grids with a grid spacing Δ are adopted to discretize the PD models. The above equation can be approximated as:

$$J_{\text{peri}} \approx \sum_{i=1}^{k_{\partial R}} W_i n_x \Delta \ -\frac{1}{2}\sum_{i=1}^{k_{R_2}}\sum_{j=1}^{k_{R_3}} [\mathrm{f}(u_{jx} - u_{ix}, x_j - x_i)\left(\frac{\partial u_x}{\partial x} + \frac{\partial \widehat{u}_x}{\partial \widehat{x}}\right) + \mathrm{f}(u_{jy} - u_{iy}, y_j - y_i)(\frac{\partial u_y}{\partial x} + \frac{\partial \widehat{u}_y}{\partial \widehat{x}})]A_j A_i$$

where *W* is the strain energy density, $\partial R$ is the integral contour,$n_x$ is the magnitude of the unit vector normal to the tangent of the contour. The sets$R_2$ and$R_3$ are the "bands" with a thickness of$\delta$ inside and outside the contour$\partial R$, respectively (see Fig. 29). *f* is the pairwise force in a PD bond connecting material points$\mathbf{x}$ and$\widehat{\mathbf{x}}$. *A* is the nodal area and $\mathbf{u}$ *is* the displacement vector.$k_{\text{all}}$ is the total number of nodes,$k_{\partial R}$ is the number of nodes along the contour$\partial R$,$k_{R_2}$ and$k_{R_3}$ are the number of nodes in the region$R_2$ and$R_3$

respectively. The domain $H$ is the horizon region.

The calculation flow for the PD J-integral is shown in Fig. 30. Given the connection between the stress intensity factor (SIF) and $J$ (J-integral),$K_{\mathrm{I}} = \sqrt{\frac{JE}{(1-\nu^2)}}$, where $E$ and$\nu$ are Young's modulus and Poisson's ratio, respectively, we can calculate the SIF by using the J-integral values obtained from the PD model.

## References


Bahrami, F., Hammad, M., Fivel, M., Huet, B., D'Haese, C., Ding, L., Nysten, B., Idrissi, H., Raskin, J., Pardoen, T., 2021. Single layer graphene controlled surface and bulk indentation plasticity in copper. Int. J. Plast. 138, 102936.

Balint, D.S., Deshpande, V., Needleman, A., Van der Giessen, E., 2008. Discrete dislocation plasticity analysis of the grain size dependence of the flow strength of polycrystals. Int. J. Plast. 24, 2149–2172.

Belytschko, T., Gracie, R., 2007. On XFEM applications to dislocations and interfaces. Int. J. Plast. 23, 1721–1738.

Bobaru, F., Yang, M., Alves, L.F., Silling, S.A., Askari, E., Xu, J., 2009. Convergence, adaptive refinement, and scaling in 1D peridynamics. Int. J. Numer. Methods Eng. 77, 852–877.

Campilho, R., Banea, M., Chaves, F., Da Silva, L., 2011. eXtended Finite Element Method for fracture characterization of adhesive joints in pure Mode I. Comput. Mater. Sci. 50, 1543–1549.

Chen, Z., Bobaru, F., 2015. Peridynamic modeling of pitting corrosion damage. J. Mech. Phys. Solids 78, 352–381.

Chen, Z., Jafarzadeh, S., Zhao, J., Bobaru, F., 2021. A coupled mechano-chemical peridynamic model for pit-to-crack transition in stress-corrosion cracking. J. Mech. Phys. Solids 146, 104203.

Chen, Z., Wang, G., Xu, Z., Li, H., Dhotel, A., Zeng, X.C., Chen, B., Saiter, J.M., Tan, L., 2013. Metal-organic frameworks capable of healing at low temperatures. Adv. Mater. 25, 6106–6111.

Cheng, Y., Cheng, C., 2004. Scaling, dimensional analysis, and indentation measurements. Mater. Sci. Eng. R Rep. 44, 91–149.

Cheng, Z., Wu, Y., Chu, L., Tang, J., Yuan, C., Feng, H., 2022. Dynamic fracture simulation of functionally graded engineered cementitious composite structures based on peridynamics. Acta Mech. Solida Sin. 35, 79–89.

Cleveringa, H., Van der Giessen, E., Needleman, A., 1999. A discrete dislocation analysis of bending. Int. J. Plast. 15, 837–868.

Cleveringa, H., Van der Giessen, E., Needleman, A., 2000. A discrete dislocation analysis of Mode I crack growth. J. Mech. Phys. Solids 48, 1133–1157.

Cordill, M., Moody, N., Gerberich, W., 2009. The role of dislocation walls for nanoindentation to shallow depths. Int. J. Plast. 25, 281–301.

Cornejo, A., Mataix, V., Zárate, F., Oñate, E., 2020. Combination of an adaptive remeshing technique with a coupled FEM–DEM approach for analysis of crack propagation problems. Comput. Part. Mech. 7, 735–752.

Creuziger, A., Bartol, L., Gall, K., Crone, W., 2008. Fracture in single crystal NiTi. J. Mech. Phys. Solids 56, 2896–2905.

Cui, Y., Wang, T., Luo, S., Li, Z., Li, Z., 2022. A discrete–continuous model of three-dimensional dislocation elastodynamics. Int. J. Plast. 152, 103221.

Curtin, W., Deshpande, V., Needleman, A., Van der Giessen, E., Wallin, M., 2010. Hybrid discrete dislocation models for fatigue crack growth. Int. J. Fatigue 32, 1511–1520.

Deshpande, V., Needleman, A., Van der Giessen, E., 2003. Finite strain discrete dislocation plasticity. J. Mech. Phys. Solids 51, 2057–2083.

Deshpande, V., Needleman, A., Van der Giessen, E., 2005. Plasticity size effects in tension and compression of single crystals. J. Mech. Phys. Solids 53, 2661–2691.

Dong, W., Liu, H., Du, J., Zhang, X., Huang, M., Li, Z., Chen, Z., Bobaru, F., 2022. A peridynamic approach to solving general discrete dislocation dynamics problems in plasticity and fracture: part I. model description and verification. Int. J. Plast., 103401

Durst, K., Backes, B., Franke, O., Göken, M., 2006. Indentation size effect in metallic materials: modeling strength from pop-in to macroscopic hardness using geometrically necessary dislocations. Acta Mater. 54, 2547–2555.

El-Awady, J.A., Biner, S.B., Ghoniem, N.M., 2008. A self-consistent boundary element, parametric dislocation dynamics formulation of plastic flow in finite volumes. J. Mech. Phys. Solids 56, 2019–2035.

Feng, H., Tang, J., Chen, H., Tian, Y., Fang, Q., Li, J., Liu, F., 2020. Indentation-induced plastic behaviour of nanotwinned Cu/high entropy alloy FeCoCrNi nanolaminate: an atomic simulation. RSC Adv. 10, 9187–9192.

Frank, F., Read Jr,, W., 1950. Multiplication processes for slow moving dislocations. Phys. Rev. 79, 722.

Galvanetto, U., Mudric, T., Shojaei, A., Zaccariotto, M., 2016. An effective way to couple FEM meshes and peridynamics grids for the solution of static equilibrium problems. Mech. Res. Commun. 76, 41–47.

Guo, X., Sun, C., Wang, C., Jiang, J., Fu, M., 2021. Study of dislocation-twin boundary interaction mechanisms in plastic deformation of TWIP steel by discrete dislocation dynamics and dislocation density-based modeling. Int. J. Plast. 145, 103076.

Hall, E., 1951a. The deformation and ageing of mild steel: II characteristics of the Lüders deformation. Proc. Phys. Soc. Lond. Sect. B 64, 742.

Hall, E., 1951b. The deformation and ageing of mild steel: III discussion of results. Proc. Phys. Soc. Lond. Sect. B 64, 747.

Hirth, J.P., 1972. The influence of grain boundaries on mechanical properties. Metall. Trans. 3, 3047–3067.

Hu, W., Ha, Y.D., Bobaru, F., Silling, S.A., 2012. The formulation and computation of the nonlocal J-integral in bond-based peridynamics. Int. J. Fract. 176, 195–206.

Hu, Z., Lynne, K., Delfanian, F., 2015. Characterization of materials' elasticity and yield strength through micro-/nano-indentation testing with a cylindrical flat-tip indenter. J. Mater. Res. 30, 578–591.

Huang, M., Huang, S., Liang, S., Zhu, Y., Li, Z., 2020. An efficient 2D discrete dislocation dynamics-XFEM coupling framework and its application to polycrystal plasticity. Int. J. Plast. 127, 102647.

Huang, M., Li, Z., Wang, C., 2007. Discrete dislocation dynamics modelling of microvoid growth and its intrinsic mechanism in single crystals. Acta Mater. 55, 1387–1396.

Jafarzadeh, S., Larios, A., Bobaru, F., 2020. Efficient solutions for nonlocal diffusion problems via boundary-adapted spectral methods. J. Peridyn. Nonlocal Model. 2, 85–110.

Jafarzadeh, S., Mousavi, F., Larios, A., Bobaru, F., 2022. A general and fast convolution-based method for peridynamics: applications to elasticity and brittle fracture. Comput. Methods Appl. Mech. Eng. 392, 114666.

Javaid, F., Stukowski, A., Durst, K., 2017. 3D Dislocation structure evolution in strontium titanate: spherical indentation experiments and MD simulations. J. Am. Ceram. Soc. 100, 1134–1145.

Juran, P., Liotier, P.-J., Maurice, C., Valiorgue, F., Kermouche, G., 2015. Investigation of indentation-, impact-and scratch-induced mechanically affected zones in a copper single crystal. C. R. Méc. 343, 344–353.

Kalácska, S., Ast, J., Ispánovity, P.D., Michler, J., Maeder, X., 2020. 3D HR-EBSD characterization of the plastic zone around crack tips in tungsten single crystals at the micron scale. Acta Mater. 200, 211–222.

Karimzadeh, A., Ayatollahi, M., Alizadeh, M., 2014. Finite element simulation of nano-indentation experiment on aluminum 1100. Comput. Mater. Sci. 81, 595–600.

Kubin, L.P., Canova, G., Condat, M., Devincre, B., Pontikis, V., Bréchet, Y., 1992. Dislocation Microstructures and Plastic Flow: A 3D Simulation, Solid State Phenomena. Trans Tech Publication, pp. 455–472.

Kuksenko, V., Roberts, S., Tarleton, E., 2019. The hardness and modulus of polycrystalline beryllium from nano-indentation. Int. J. Plast. 116, 62–80.

Le, Q., Bobaru, F., 2018. Surface corrections for peridynamic models in elasticity and fracture. Comput. Mech. 61, 499–518.

Lehoucq, R., Silling, S., 2008. Force flux and the peridynamic stress tensor. J. Mech. Phys. Solids 56, 1566–1577.

Liang, S., Huang, M., Zhao, L., Zhu, Y., Li, Z., 2021. Effect of multiple hydrogen embrittlement mechanisms on crack propagation behavior of FCC metals: competition vs. synergy. Int. J. Plast. 143, 103023.
Liang, S., Zhu, Y., Huang, M., Li, Z., 2019. Simulation on crack propagation vs. crack-tip dislocation emission by XFEM-based DDD scheme. Int. J. Plast. 114, 87–105.
Liu, B., Eisenlohr, P., Roters, F., Raabe, D., 2012. Simulation of dislocation penetration through a general low-angle grain boundary. Acta Mater. 60, 5380–5390.
Liu, Q., Fang, L., Xiong, Z., Yang, J., Tan, Y., Liu, Y., Zhang, Y., Tan, Q., Hao, C., Cao, L., 2021. The response of dislocations, low angle grain boundaries and high angle grain boundaries at high strain rates. Mater. Sci. Eng. A 822, 141704.
Longsworth, M., Fivel, M., 2021. The effect of stress on the cross-slip energy in face-centered cubic metals: a study using dislocation dynamics simulations and line tension models. J. Mech. Phys. Solids 148, 104281.
Lu, S., Kan, Q., Zaiser, M., Li, Z., Kang, G., Zhang, X., 2022. Size-dependent yield stress in ultrafine-grained polycrystals: a multiscale discrete dislocation dynamics study. Int. J. Plast. 149, 103183.
Lu, S., Zhang, B., Li, X., Zhao, J., Zaiser, M., Fan, H., Zhang, X., 2019. Grain boundary effect on nanoindentation: a multiscale discrete dislocation dynamics model. J. Mech. Phys. Solids 126, 117–135.
Mei, T., Zhao, J., Liu, Z., Peng, X., Chen, Z., Bobaru, F., 2021. The role of boundary conditions on convergence properties of peridynamic model for transient heat transfer. J. Sci. Comput. 87, 1–22.
Mousavi, F., Jafarzadeh, S., Bobaru, F., 2021. An ordinary state-based peridynamic elastoplastic 2D model consistent with J2 plasticity. Int. J. Solids Struct. 229, 111146.
Oswald, J., Wintersberger, E., Bauer, G., Belytschko, T., 2011. A higher-order extended finite element method for dislocation energetics in strained layers and epitaxial islands. Int. J. Numer. Methods Eng. 85, 920–938.
Pagani, A., Carrera, E., 2020. Coupling three-dimensional peridynamics and high-order one-dimensional finite elements based on local elasticity for the linear static analysis of solid beams and thin-walled reinforced structures. Int. J. Numer. Methods Eng. 121, 5066–5081.
Peach, M., Koehler, J., 1950. The forces exerted on dislocations and the stress fields produced by them. Phys. Rev. 80, 436.
Pharr, G.M., Herbert, E.G., Gao, Y., 2010. The indentation size effect: a critical examination of experimental observations and mechanistic interpretations. Annu. Rev. Mater. Res. 40, 271–292.
Segurado, J., LLorca, J., Romero, I., 2007. Computational issues in the simulation of two-dimensional discrete dislocation mechanics. Modelling and Simulation in. Mater. Sci. Eng. 15, S361.
Shim, S., Bei, H., George, E.P., Pharr, G.M., 2008. A different type of indentation size effect. Scr. Mater. 59, 1095–1098.
Shinde, A.B., Patil, S., Patil, P., Salunkhe, R., Sande, R., Pawar, S., Patil, V., 2022. Dislocation and deformation analysis of Cu-Ni thin films during Nano-indentation using molecular dynamics simulation approach. Mater. Today Proc. 49, 1453–1461.
Silling, S.A., 2000. Reformulation of elasticity theory for discontinuities and long-range forces. J. Mech. Phys. Solids 48, 175–209.
Silling, S.A., Askari, A., 2014. Peridynamic Model for Fatigue Cracking. Sandia National Laboratories, Albuquerque. SAND-18590.
Song, K., Wang, K., Zhang, L., Zhao, L., Xu, L., Han, Y., Hao, K., 2022. Insights on low cycle fatigue crack formation and propagation mechanism: a microstructurally-sensitive modeling. Int. J. Plast. 154, 103295.
Sumigawa, T., Byungwoon, K., Mizuno, Y., Morimura, T., Kitamura, T., 2018. In situ observation on formation process of nanoscale cracking during tension-compression fatigue of single crystal copper micron-scale specimen. Acta Mater. 153, 270–278.
Sylwestrowicz, W., Hall, E., 1951. The deformation and ageing of mild steel. Proc. Phys. Soc. Lond. Sect. B 64, 495.
Takahashi, A., Ghoniem, N.M., 2008. A computational method for dislocation-precipitate interaction. J. Mech. Phys. Solids 56, 1534–1553.
Thompson, A.W., Baskes, M.I., Flanagan, W.F., 1973. The dependence of polycrystal work hardening on grain size. Acta Metall. 21, 1017–1028.
Van der Giessen, E., Needleman, A., 1995. Discrete dislocation plasticity: a simple planar model. Modell. Simul. Mater. Sci. Eng. 3, 689.
Wang, C., Sun, C., Cai, W., Qian, L., Guo, X., Fu, M., 2022. Evolution of partial dislocation slip–mediated deformation twins in single crystals: a discrete dislocation plasticity model and an analytical approach. Int. J. Plast. 152, 103230.
Wang, Q., Wu, M., Zhang, C., Lv, Y., Ji, X., 2019a. Effect of machining-induced subsurface defects on dislocation evolution and mechanical properties of materials via nano-indentation. Nanoscale Res. Lett. 14, 1–13.
Wang, X.Q., Chow, C.L., Lau, D., 2019b. A review on modeling techniques of cementitious materials under different length scales: development and future prospects. Adv. Theory Simul. 2, 1900047.
Wu, P., Yang, F., Chen, Z., Bobaru, F., 2021. Stochastically homogenized peridynamic model for dynamic fracture analysis of concrete. Eng. Fract. Mech. 253, 107863.
Wu, P., Zhao, J., Chen, Z., Bobaru, F., 2020. Validation of a stochastically homogenized peridynamic model for quasi-static fracture in concrete. Eng. Fract. Mech. 237, 107293.
Xu, Y., Balint, D., Dini, D., 2019. A new hardness formula incorporating the effect of source density on indentation response: a discrete dislocation plasticity analysis. Surf. Coat. Technol. 374, 763–773.
Xu, Z., Zhang, G., Chen, Z., Bobaru, F., 2018. Elastic vortices and thermally-driven cracks in brittle materials with peridynamics. Int. J. Fract. 209, 203–222.
Yang, X., Zhai, H., Ruan, H., Shi, S., Zhang, T., 2018. Multi-temperature indentation creep tests on nanotwinned copper. Int. J. Plast. 104, 68–79.
Zambaldi, C., Raabe, D., 2010. Plastic anisotropy of γ-TiAl revealed by axisymmetric indentation. Acta Mater. 58, 3516–3530.
Zhang, G., Gazonas, G.A., Bobaru, F., 2018. Supershear damage propagation and sub-Rayleigh crack growth from edge-on impact: a peridynamic analysis. Int. J. Impact Eng. 113, 73–87.
Zhang, Y., Gao, Y., Nicola, L., 2014. Lattice rotation caused by wedge indentation of a single crystal: dislocation dynamics compared to crystal plasticity simulations. J. Mech. Phys. Solids 68, 267–279.
Zhang, Y., Mohanty, D.P., Seiler, P., Siegmund, T., Kruzic, J.J., Tomar, V., 2017. High temperature indentation based property measurements of IN-617. Int. J. Plast. 96, 264–281.
Zhou, N., Elkhodary, K.I., Huang, X., Tang, S., Li, Y., 2020. Dislocation structure and dynamics govern pop-in modes of nanoindentation on single-crystal metals. Philos. Mag. 100, 1585–1606.
Zhu, Q., Huang, Q., Guang, C., An, X., Mao, S.X., Yang, W., Zhang, Z., Gao, H., Zhou, H., Wang, J., 2020. Metallic nanocrystals with low angle grain boundary for controllable plastic reversibility. Nat. Commun. 11, 1–8.